Supporting Information for:

Growth Kinetics Determine the Polydispersity and Size of PbS and PbSe Nanocrystals

Michael P. Campos[$,‡] Jonathan de Roo[$+,‡] Matthew W. Greenberg[$,‡] Brandon M. McMurtry[$,‡] Mark P. Hendricks[$], Ellie Bennett[$], Natalie Saenz[$], Matthew Y. Sfeir[‖#^], Benjamin Abécassis[Ω§], Sanjit K. Ghose[⊥], and Jonathan S. Owen[$*]

[$]Department of Chemistry, Columbia University, New York, New York 10027.

[+] Department of Chemistry, University of Basel, Basel 4058, Switzerland.

[‖] Center for Functional Nanomaterials, Brookhaven National Laboratory, Upton, New York 11973.

[#] Photonics Initiative, Advanced Science Research Center, City University of New York, New York, New York 10031.

[^] Department of Physics, Graduate Center, City University of New York, New York, New York 10016.

[Ω] Laboratoire de Chimie, ENS de Lyon, CNRS, Université Claude Bernard Lyon 1, F69342, Lyon, France.

[§] Université Paris-Saclay, CNRS, Laboratoire de Physique des Solides, 91405 Orsay, France.

[⊥] National Synchrotron Light Source II, Brookhaven National Laboratory, Brookhaven, New York,

* Corresponding author: jso2115@columbia.edu

‡ These authors contributed equally

Sections:

Section 1: Supplementary figures (S1–S5)

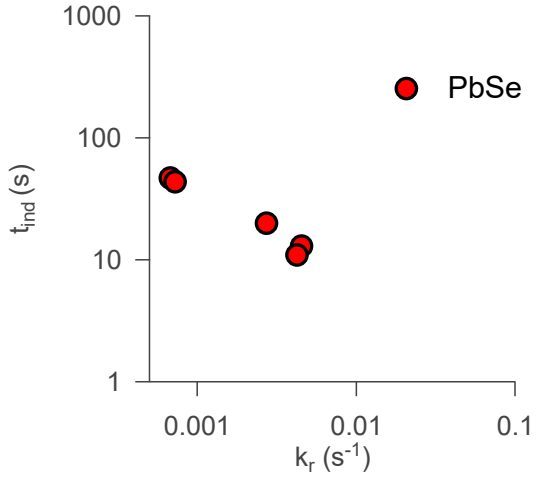

Figure S1. Induction delay as a function of first order rate constant at 90 °C.

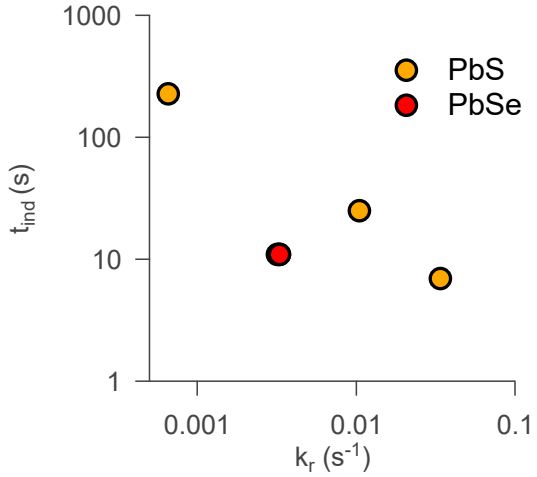

Figure S2. Induction delay as a function of first order rate constant at 100 °C.

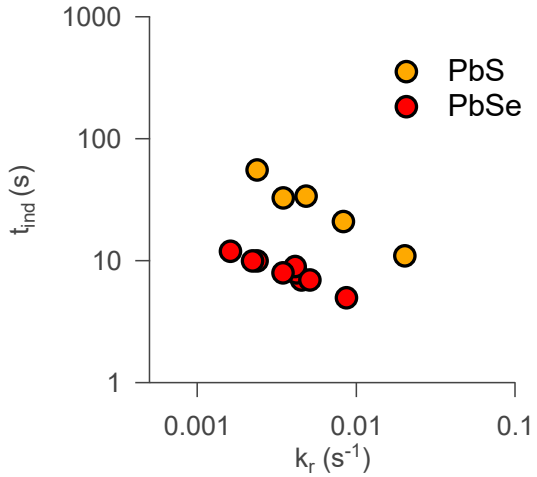

Figure S3. Induction delay as a function of first order rate constant at 110 °C.

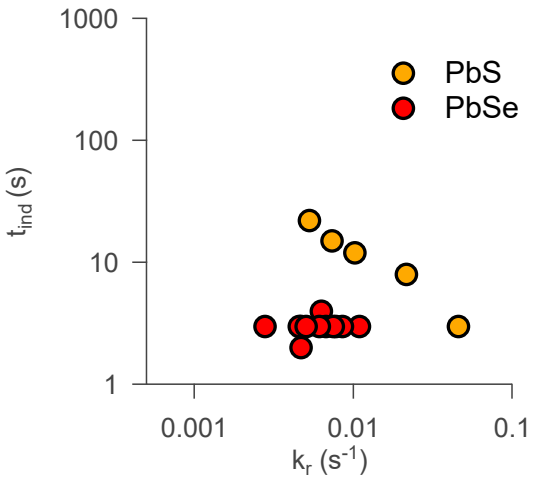

Figure S4. Induction delay as a function of first order rate constant at 120 °C.

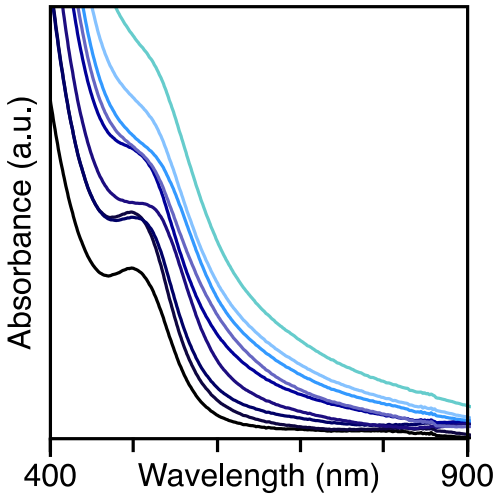

Figure S5. UV-Vis-NIR spectra of reaction aliquots shown in Figure 6A plotted to clearly show the cluster feature at $\lambda \sim$ 475-510 nm.

Section 2: Experimental details

General methods

All manipulations were performed using standard air-free techniques on a Schlenk line under an argon atmosphere or in a nitrogen-filled glovebox, unless otherwise indicated.

Chemicals

Toluene (99.5%), phenyl isothiocyanate (98%), 4-(trifluoromethyl)phenyl isothiocyanate (97%), and dodecylamine (98%) were obtained from Aldrich and used without further purification. 3,5-*bis*(trifluoromethyl)phenyl isothiocyanate (97+%) was obtained from Maybridge and used without further purification. Tetrachloroethylene (anhydrous, ≥99%) and diglyme (anhydrous, 99.5%) were obtained from Aldrich, transferred to a nitrogen-filled glovebox, shaken with activated alumina, filtered, and stored over activated 3 Å molecular sieves for 24 hours prior to use. Hexadecane (99%) and diphenyl ether (≥99%) were obtained from Aldrich, stirred with calcium hydride overnight, distilled under vacuum (30 mtorr), transferred to a nitrogen-filled glovebox, and stored over activated 3 Å molecular sieves for 24 hours prior to use. *o*-toluidine (≥99%) and 2-isopropylaniline (97%) were obtained from Aldrich, distilled under vacuum (30 mtorr), and stored in a nitrogen-filled glovebox prior to use.

New thioureas

Lead oleate and thiourea syntheses were carried out according to Hendricks *et. al*. Selenourea syntheses were carried out according to Campos *et. al*.[1-2]

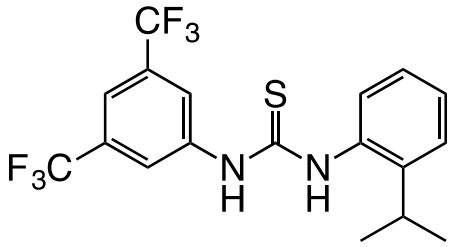

***N*-(3,5-bis(trifluoromethyl)phenyl)-*N'*-(2-isopropylphenyl)thiourea (*TU(3,5-(CF$_3$)$_2$Ph,2-i*PrPh)*)**. White powder. Recrystallized by addition of hexanes to a saturated solution in dichloromethane. Isolated by suction filtration and dried under vacuum >3 hours. ^{1}H NMR (C_6D_6, 500 MHz): δ = 0.97 (d, $J_{H\text{-}H}$ = 6.9 Hz, 6H, CH_3), 3.00 (sept., $J_{H\text{-}H}$ = 6.9 Hz, 1H, isopropyl CH), 6.84 (m, 3H, aryl CH), 7.00 (m, 2H, aryl CH), 7.47 (s, 1H, NH), 7.64 (s, 2H, aryl CH), 8.09 (br s, 1H, NH). ^{13}C{^{1}H} (125 MHz, C_6D_6): δ = 22.9 (CH_3), 28.2 (isopropyl CH), 118.9 (aryl CH or $CF_2\underline{C}HCF_3$), 123.2 (CF_3, q, $J_{C\text{-}F}$ = 272.8 Hz), 124.8 (aryl CH or $CF_2\underline{C}HCF_3$), 127.1 (aryl CH), 127.2 (aryl CH), 129.2 (CH), 131.5 ($\underline{C}CF_3$, q, $J_{C\text{-}F}$ = 33 Hz), 133.0 (*i*-C), 140.0 (*i*-C), 146.2 ($\underline{C}CH(CH_3)_2$), 180.7 (C(S)). Anal. Calcd for $C_{18}H_{16}F_6N_2S$: C, 53.20; H, 3.97; N, 6.89.

Found: C, 53.05; H, 3.74; N, 6.78. MS (ASAP) *m/z* Calcd for [$C_{18}H_{16}F_6N_2{}^{32}S + H^+$]: 407.1017. Found: 407.1016.

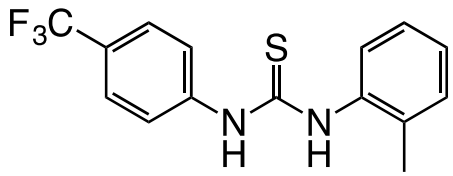

***N*-(*o*-tolyl)-*N'*-(4-(trifluoromethyl)phenyl)thiourea (*TU(4-CF$_3$Ph,2-MePh)*).** White powder. ^{1}H NMR (C_6D_6, 500 MHz): δ = 3.01 (s, 3H, CH_3), 6.87-6.95 (m, 4H, aryl CH), 7.09 (m, 2H, aryl CH), 7.17 (m, 2H, aryl CH), 7.52 (br, 1H, NH), 8.29 (br, 1H, NH). ^{13}C{^{1}H} (125 MHz, C_6D_6): δ = 17.80 (CH_3), 123.68 (aryl CH), 124.76 (q, $J_{C\text{-}F}$ = 271.6 Hz, CF_3), 126.08 (q, $J_{C\text{-}F}$ = 3.8 Hz, $\underline{C}HCCF_3$), 127.29 (q, $J_{C\text{-}F}$ = 32.5 Hz, $\underline{C}CF_3$), 127.46 (aryl CH), 128.51 (aryl CH), 131.69 (aryl CH), 135.52 (*i*-C), 135.81 (*i*-C), 141.66 (*i*-C), 180.15 (C(S)). Anal. Calcd for $C_{15}H_{13}F_3N_2S$: C, 58.05; H, 4.22; N, 9.03. Found: C, 58.06; H, 4.11; N, 9.01. MS (ASAP) *m/z* Calcd for [$C_{15}H_{13}F_3N_2{}^{32}S + H^+$]: 311.0830. Found: 311.0831.

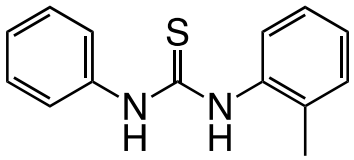

***N*-phenyl-*N'*-(*o*-tolyl)thiourea (*TU(2-MePh,Ph)*).** White powder. ^{1}H NMR ($CDCl_3$, 500 MHz): δ = 2.34 (s, 3H, CH_3), 7.25-7.32 (m, 4H, aryl CH), 7.36-7.42 (m, 5H, aryl CH), 7.93 (br s, 2H, NH). ^{13}C{^{1}H} (125 MHz, C_6D_6): δ = 18.07 (CH_3), 125.46 (aryl CH), 127.02 (aryl CH), 127.29 (aryl CH), 127.86 (aryl CH), 128.44 (aryl CH), 129.47 (aryl CH), 131.47 (aryl CH), 135.45 (*i*-C), 135.52 (*i*-C), 137.47 (*i*-C), 180.47 (C(S)). Anal. Calcd for $C_{14}H_{14}N_2S$: C, 69.39; H, 5.82; N, 11.56. Found: C, 69.34; H, 5.61; N, 11.52. MS (ASAP) *m/z* Calcd for [$C_{14}H_{14}N_2{}^{32}S + H^+$]: 243.0956. Found: 243.0958.

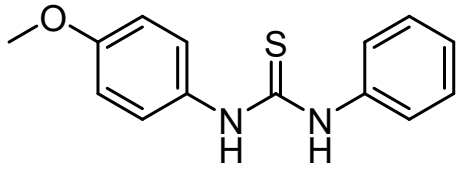

***N*-phenyl-*N'*-(*p*-methoxyphenyl)thiourea (*TU(2-OMePh,Ph)*).** White powder. Synthesized from *p*-anisidine and phenyl isothiocyanate. The product precipitates as a white powder from the reaction and is isolated by vacuum filtration over a fine frit where it is washed with 100 mL hexanes and then dried overnight. ^{1}H NMR (CD_3CN, 500 MHz): δ = 3.79 (s, 3H, CH3), 6.94 (m, 2H, aryl CH), 7.22 (m, 1H, aryl CH), 7.28 (m, 2H, aryl CH), 7.38 (m, 4H, aryl CH), 8.16 (br s, 2H, NH). ^{13}C{^{1}H} (125 MHz, CD_3,CN): δ = 56.09 (CH_3), 115.12 (aryl CH), 126.35 (aryl CH), 126.86 (aryl CH), 128.55 (aryl CH), 129.79 (aryl CH), 131.90 (aryl CH), 139.59 (*i*-C), 159.16 (aryl CH), 182.15 (C(S)). Anal. Calcd for $C_{14}H_{14}N_2OS$: C, 65.09; H, 5.46; N, 10.84.

Found: C, 65.00; H, 5.47; N, 10.83. MS (ASAP) *m/z* Calcd for [$C_{14}H_{14}N_2O^{32}S + H^+$]: 259.0906. Found: 259.0905.

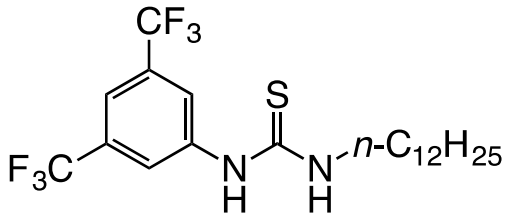

***N*-(3,5-*bis*(trifluoromethyl)phenyl)-*N'*-dodecylthiourea (*TU(3,5-(CF$_3$)$_2$Ph,C12)*).** White powder. ^{1}H NMR (C_6D_6, 500 MHz): δ = 0.92 (t, J_{H-H} = 7.1 Hz, 3H, CH_3), 1.09-1.35 (m, 20H, CH_2), 3.37 (br, 2H, α-CH_2), 5.41 (br, 1H, NH), 7.40 (s, 2H, aryl CH), 7.44 (s, 1H, aryl CH), 7.56 (br, 1H, NH). ^{13}C{^{1}H} (125 MHz, C_6D_6): δ = 14.38 (CH_3), 23.15 (CH_2), 27.33 (CH_2), 28.95 (CH_2), 29.70 (CH_2), 29.85 (CH_2), 29.98 (CH_2), 30.05 (CH_2), 30.13 (CH_2), 30.15 (CH_2), 32.37 (CH_2), 45.43 (α-CH_2), 118.38 (m, aryl CH), 132.20 (m, aryl CH), 123.46 (q, J_{C-F} = 273.0 Hz, CF_3), 132.77 (q, J_{C-F} = 33.5 Hz, $\underline{C}CF_3$), 139.83 (*i*-C), 180.77 (C(S)). Anal. Calcd for $C_{21}H_{30}F_6N_2S$: C, 55.25; H, 6.62; N, 6.14. Found: C, 55.24; H, 6.89; N, 6.11. MS (ASAP) *m/z* Calcd for [$C_{21}H_{30}F_6N_2{}^{32}S + H^+$]: 457.2112. Found: 457.2110.

Fitting of *in situ* PDF data to candidate PbS solute structures.

Discrete Debye Scattering Equation based calculations were performed using the DiffpyCMI complex modeling framework using DebyePDFGenerator.[3] The structures are refined using least squares analysis with isotropic ADPs on Pb, S, O, a scale factor, a quadratic correlated motion correction for relative low-*r* peak intensities, and an isotropic stretching factor of the XYZ coordinate matrix as variables in the fit. Structural optimizations were carried out using DFT implemented in the Jaguar 9.1 suite of *ab initio* quantum chemistry programs.[4] Geometry optimizations were performed with the MO6-2X functional using the LACVP** basis set.[5] The absence of imaginary frequencies in the calculated harmonic vibrational frequencies were used to confirm that the calculated geometries represent minima on the potential energy surface. Initial guesses for the geometry were generated by molecular mechanics as implemented in Avogadro version 1.2.0 using the UFF force field.[6]

Estimation of error in [NC].

The [NC] was determined using a previously determined size-dependent extinction coefficient, as described in the Experimental section of this manuscript. Therefore, the almost all of the uncertainty in [NC] will derive from error in the extinction coefficient we used. As with most extinction coefficient measurements, the largest source of error arises from the nanocrystal size

measurement. To account for this, we estimated an error of two monolayers (~0.6 nm) in the nanocrystal diameter. Propagating this to an uncertainty in the nanocrystal volume we arrive at an error between 20-40%, with the percent error decreasing with nanocrystal size. Using this error in the nanocrystal volume we estimated the [NC] as shown in Figure 6B.

Section 3: Comment on k_r fit quality

The single exponential fit is an approximation since the exact rate law is not known. However, the single exponential describes the data quite well. As mentioned previously, the overall fit provides a good description of most of the data and provides a reliable estimate of the reaction rate constant. However, t_{ind} is very sensitive to small changes in the fit and often the residuals are highest at the early time points (Figure S6A and S6C).

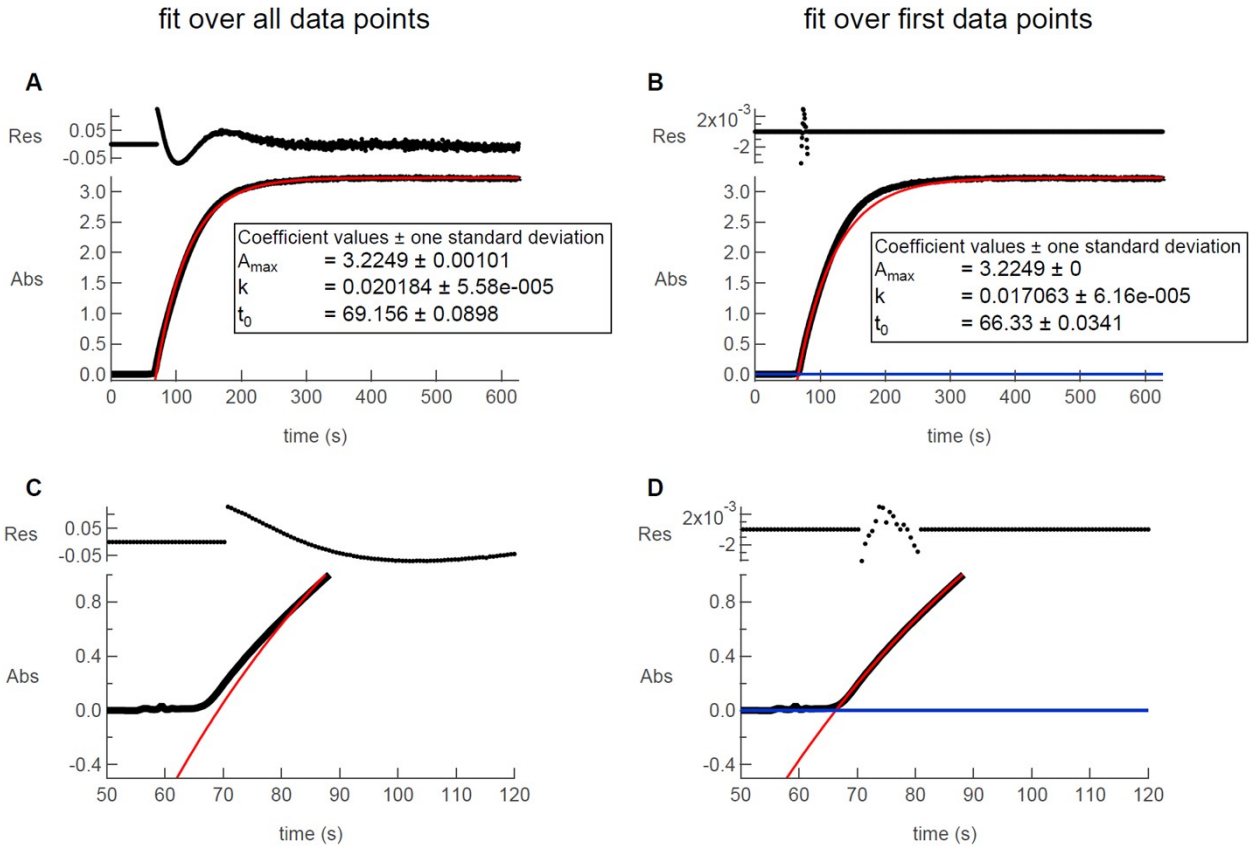

Figure S6. Difference between overall fit and early time points fit.

In extreme cases, for short induction times, t_{ind} can be smaller than t_{inj}, leading to negative induction times. Therefore, to correctly identify t_{ind}, the algorithm applies another fit over the early time points (Figure S6B and S6D). Of course, this leads to a slightly different rate constant. However, the average variability is about 10 % and for most data sets, the variability is under 20 % (see Figure S7 for a histogram of the variability).

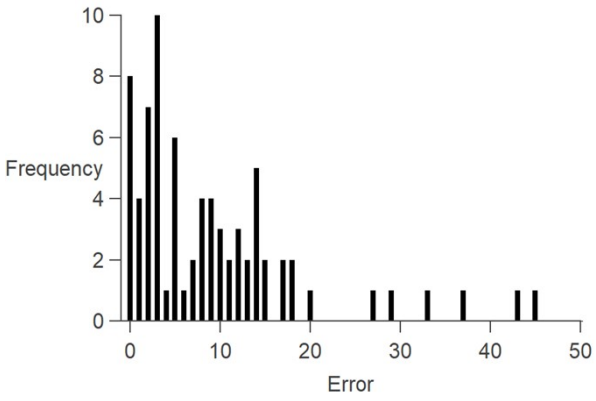

Figure S7. Histogram of the variability on the rate constant between the overall and early time point fit.

Section 4: Setup and collection of *in situ* X-ray total scattering measurements

Experimental Set Up

The peristaltic pump which flows the reaction solution in front of the beathpath is controlled externally outside the hutch with custom written code. Briefly, the injection of the S/Se precursor is remotely triggered and then the persitaltic pump is run on max setting for ten seconds to ensure the solution has flowed through the entire flow cell prior to acquisition. Then the pump is set to a slower speed and the acquisition of X-ray diffraction patterns is initiated. The total solution volume of the viton tubing between the flask and the X-ray beam is approximately 2 mL. This leads to a dead time of 30 seconds for the PbS and PbSe reaction conditions respectively. During the period following the beginning of acquisitions the acquired 30 second diffraction pattern(s) are of the reaction solution which was pumped out while the pump was operating in fast mode. Therefore, we have corrected the timing to reflect the fact that the acquisition during this dead time reflects the reaction solution which was pumped out between 10-15 seconds following initiation of the reaction in the flask. Given the likelyhood that the reaction still proceeds to some extent in the Viton tubing, and these scans represent averaged diffraction intensities over the whole 30 second acquisition period these “in flask” reaction times are an approximation. This approximation is necessitated by the finite time needed to acquire sufficient S/N to produce diffuse scattering data which can be meaningfully used to generate a PDF as well as the need for a relatively slow pump rate to allow for data collection over an extended period of time without recirculating the solution.

Figure S8. Custom designed X-ray Flow Cell benchmarked at NSLS-II 28-ID-2 beamline. A remotely triggered injector initiates the nanoparticle reaction by injecting a syringe of the

chalcogenourea precursor into a hot lead oleate solution. Then, a peristaltic pump flows the nanocrystal solution in front of the X-Ray beam path allowing for time resolved diffraction measurements of the evolving nanocrystal reaction solution.

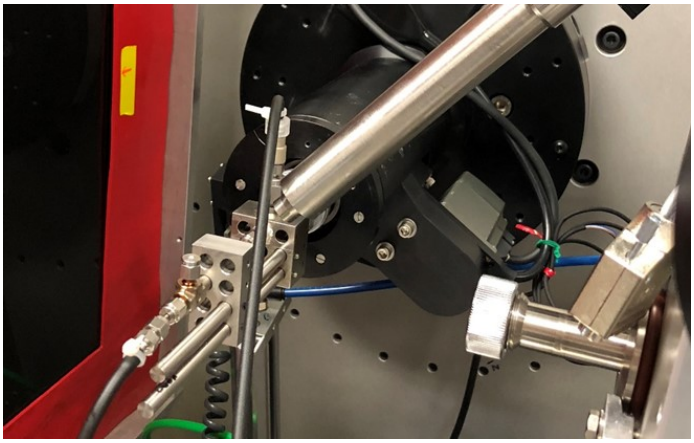

Figure S9. Custom designed X-ray flow cell, the solution is flowed through kapton tubing which is aligned with the X-ray beam.

Total Scattering Structure Function, S(Q), Raw Data

The nominal composition for normalization of the total scattering structure function $S(Q) = \frac{I(Q)_{coh} + \langle f(Q)\rangle^2 - \langle f^2(Q)\rangle}{\langle f(Q)\rangle^2}$ was chosen to be "PbS" or "PbSe" for *in-situ* nanocrystal reactions which form PbS or PbSe respectively. $f(Q)$ is the Q dependent X-Ray form factor.[7] In the case of lead oleate this was chosen to be the molecular formula of lead oleate.

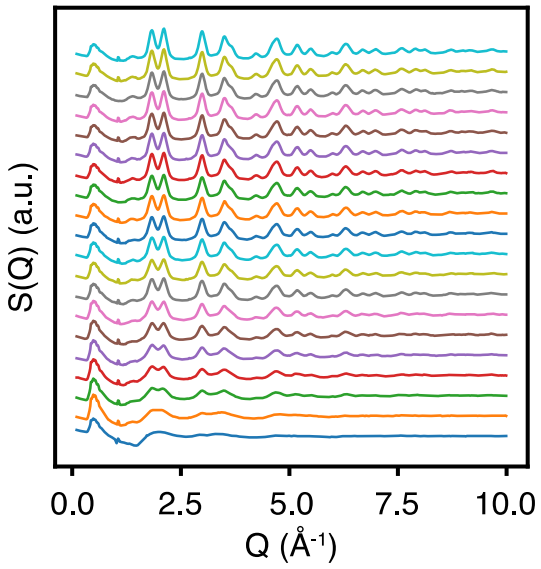

Figure S10. *In-situ* total scattering structure function, S(Q), of a PbS nanoparticle reaction with 30 second scans intervals.

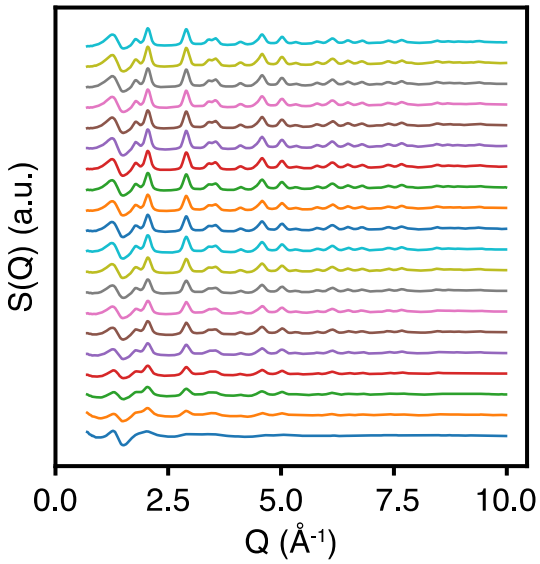

Figure S11. *In-situ* total scattering structure function, S(Q), of a PbSe nanoparticle reaction with 30 second scans intervals.

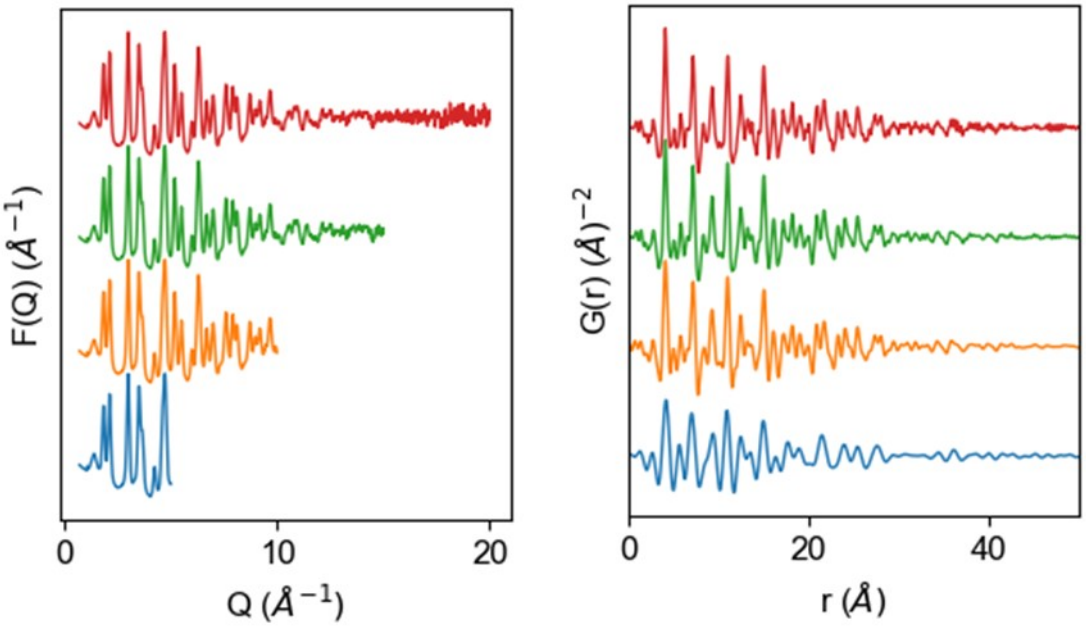

Figure S12. PbS nanoparticle reaction timepoints at late times process with varying ranges of $F(Q)$ (left) used in the Fourier transform to generate $G(r)$ (right). A Q_{max} of 10 Å^{-1} is accessible throughout the reaction.

Section 5: Virtual crystal modeling of PbS and PbSe nanocrystal formation

To model the time dependent evolution of the PDF $G(r,t)$ we have applied an established treatment of the finite size effects of nanocrystals on the pair distribution function.[8-9] The PDF is modeled as the PDF of the bulk lattice multiplied by a spherical envelope function $f(r,d)$ dependent on nanocrystal diameter d as $G(r,d) = G(r)_{bulk} * f(r,d)$. Specifically,

$$f(r,d) = \left[1 - \frac{3r}{2d} + \frac{1}{2}\left(\frac{r}{d}\right)^3\right] * h(d-r) \quad \text{(S2)}$$

where $h(d-r)$ is the heaviside step function which is zero for r greater than d, and 1 for $r \leq d$.[10] In this case, $G(r)_{bulk}$ is the rock salt PbS or PbSe lattice. Fitting parameters related to experimental resolution – the finite Q space resolution gaussian dampening factor Q_{damp} as well as the empirical broadening factor Q_{broad} – were acquired by fitting the PDF of a Ni standard taken in the same size Kapton tubing as that used in the flow cell in the same sample orientation. Correlated atomic motion was treated by optimizing an empirical quadratic correlated atomic motion correction factor, δ_2, which was fit using the PDF of the final nanocrystal product. The atomic displacement parameters of Pb and S/Se atoms in the nanocrystalline product were refined for the final nanocrystal only to prevent overparameterization of the model during fitting of the full time series. The resulting real space guassian peak width correction factor to a correlation at separation r_{ij} is

$$\sigma_{ij} = \sigma_{ij}^{'} \sqrt{1 - \frac{\delta_2}{r_{ij}^2} + Q_{broad}^2 * r_{ij}^2} \quad \text{(S3)}$$

where $\sigma_{ij}^{'}$ is the uncorrelated peak width calculated from the atomic displacement parameters of the atoms at positions i and j.[11-12]

In order to fit each timepoint to best match the experimental data in the reaction, three parameters are refined using least-squares refinement implemented in PDFgui – a scale factor, a nanocrystal diameter d, and the cubic lattice constant of the rock salt lattice.[12] The goodness of fit is quantified by the residual fit function

$$R_w = \sqrt{\frac{\sum_{i=1}^{n}[G_{obs}(r_i) - G_{calc}(r_i)]^2}{\sum_{i=1}^{n} G_{obs}(r_i)^2}} \quad \text{(S4)}$$

It is seen that the R_w as a function of time, $R_w(t)$, quickly approaches low values indicative of a good fit to a nanocrystal proxy model several minutes following nucleation in each case and asymptotically approaches the final value (Figure S13A). The time evolution of $R_w(t)$ which shows poor agreement at early times to the nanocrystal proxy model (Figure S13B) and excellent agreement at latter times is indicative of the progression from a $(PbS)_x(Pb(oleate)_2)_y$ solute to final rock salt PbS nanocrystal products.

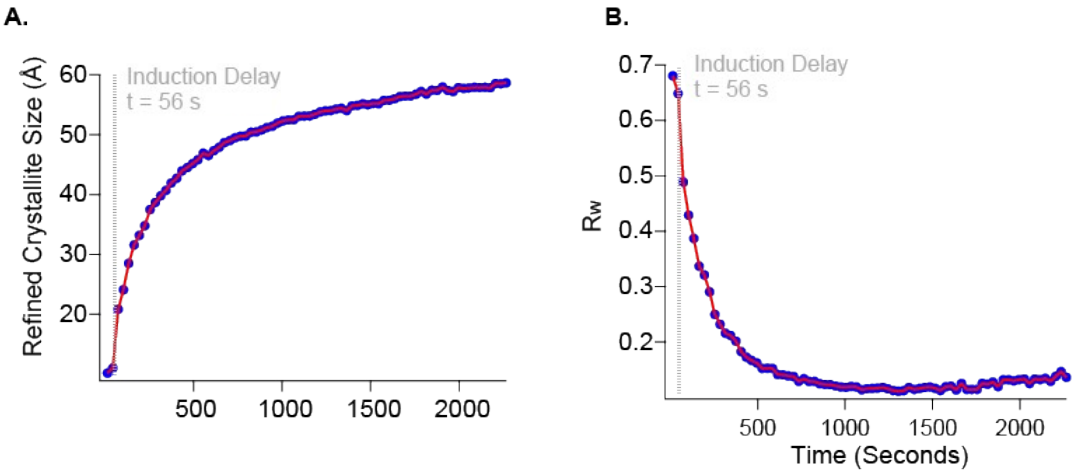

Figure S13. Refined parameters from virtual crystal modeling fitting of 110 °C *in-situ* PbS reaction. (A) Temporal evolution of the spherical envelope function diameter (*i.e.*, size of rock salt crystalline domains) and (B) $R_w(t)$.

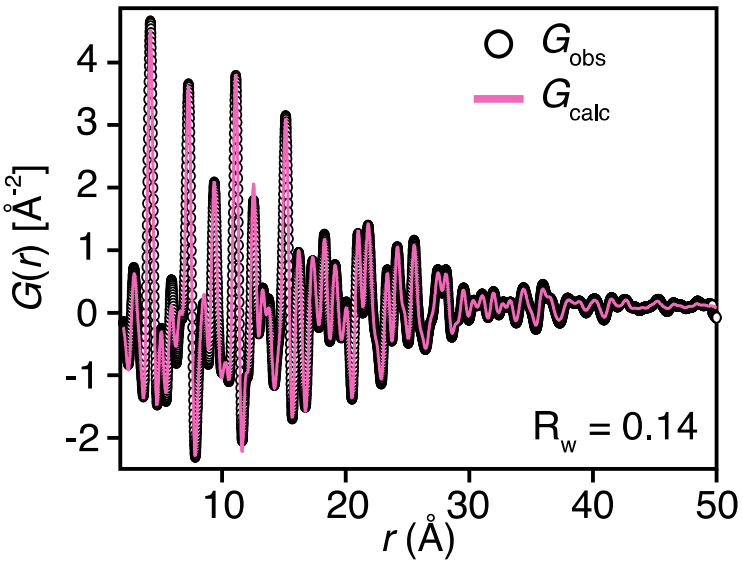

Figure S14. Observed and best fit (nanoparticle model) calculated reduced PDF pattern for the final product of an *in-situ* PbS reaction run at 110 °C.

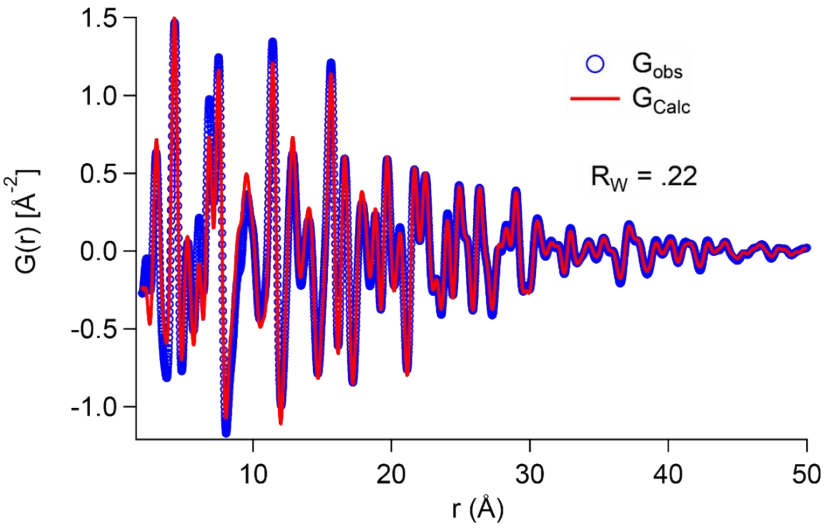

Figure S15. Observed and best fit (nanoparticle model) calculated reduced PDF pattern for the final product of an in-situ PbSe reaction run at 110 °C.

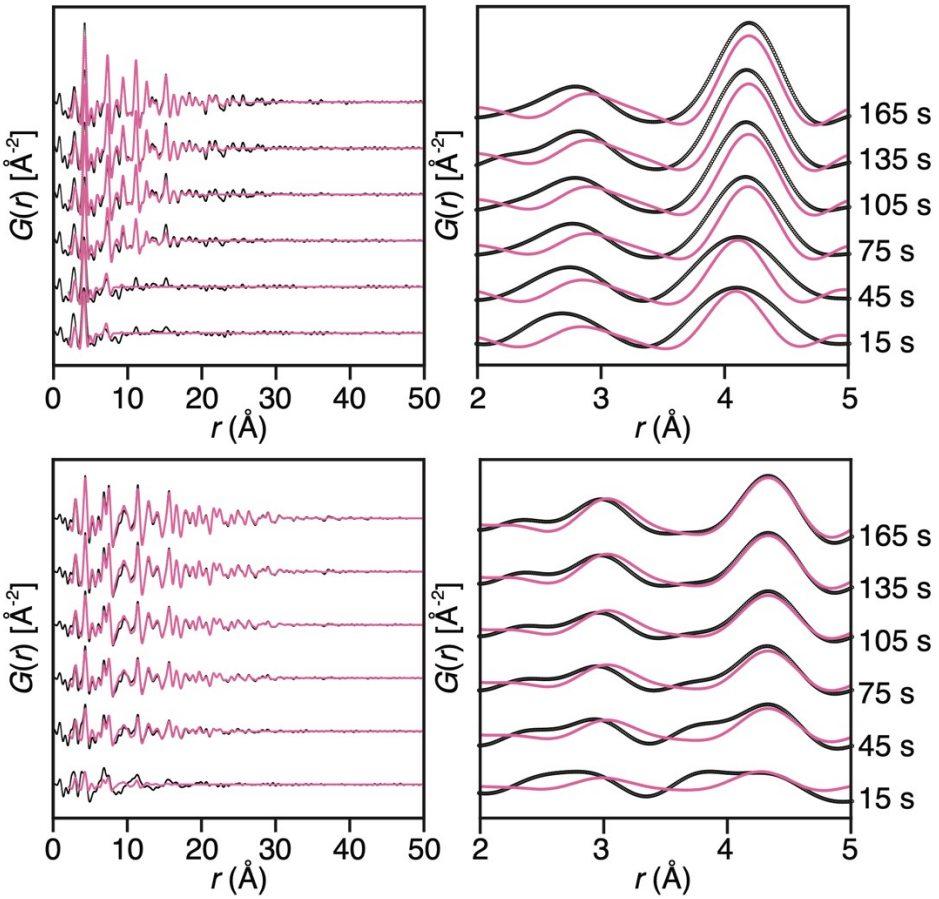

Figure S16. Early time PbS (top) and PbSe (bottom) PDF patterns as shown in Figure 4 (black) and fits using virtual crystal models of the respective materials (pink). We note the poor fit of both virtual crystal models to the collected PDF patterns at early times. Low-*r* data for each material is also shown, highlighting the differences in both relative peak intensities and peak positions of the experimental local structure (first nearest neighbor and second nearest correlations) to the virtual crystal model at early times.

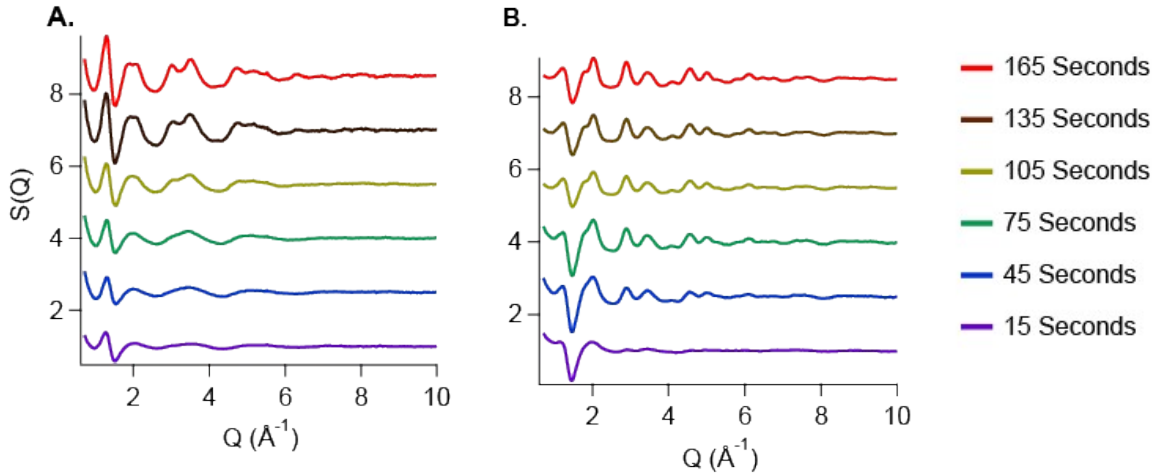

Figure S17. Total scattering structure function of early timepoints of *in-situ* X-Ray measurements for (A) PbS and (B) PbSe nanocrystal reactions at 80 °C with similar precursor conversion kinetics.

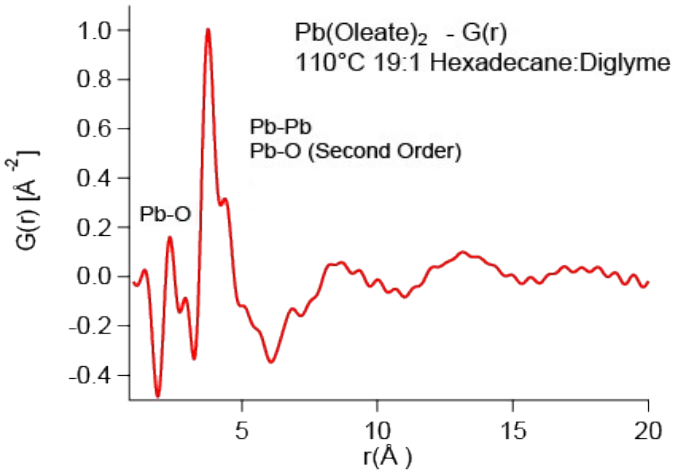

Figure S18. Reduced pair distribution function of lead(II) oleate in reaction solution.

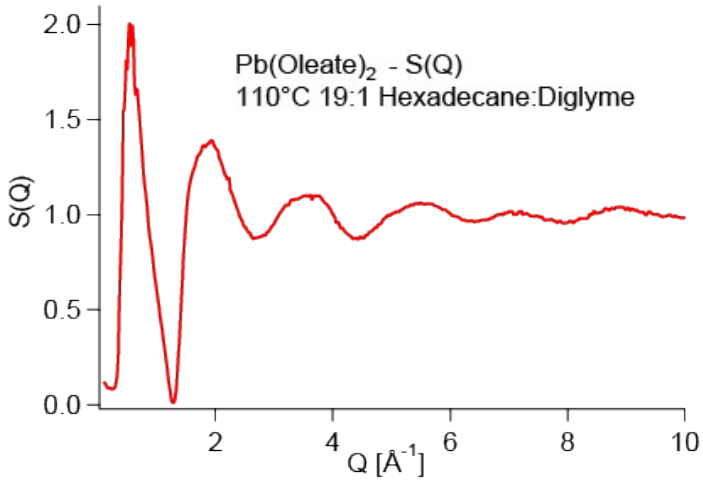

Figure S19. Total scattering structure function of lead(II) oleate in reaction solution.

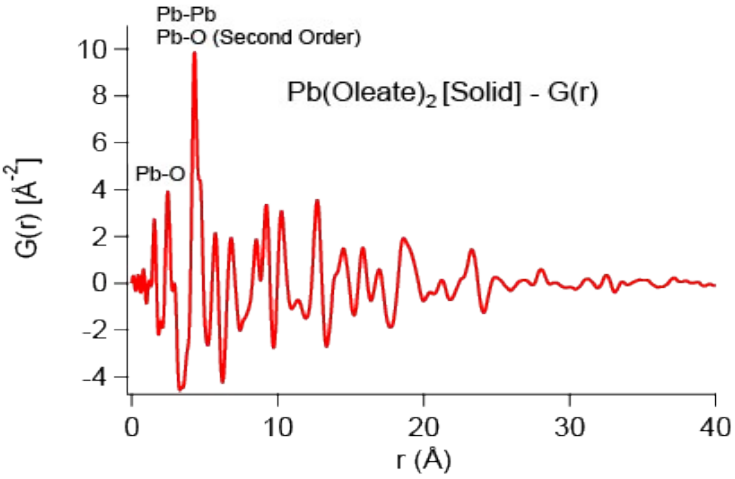

Figure S20. Reduced pair distribution function of solid lead(II) oleate at room temperature.

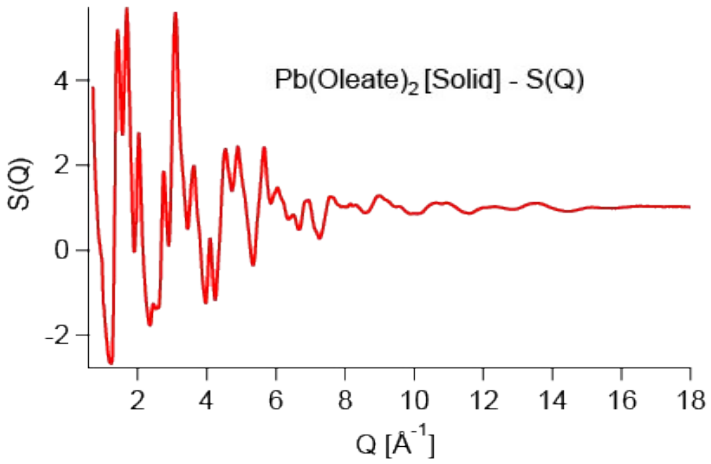

Figure S21. Total scattering structure function of solid lead(II) oleate at room temperature.

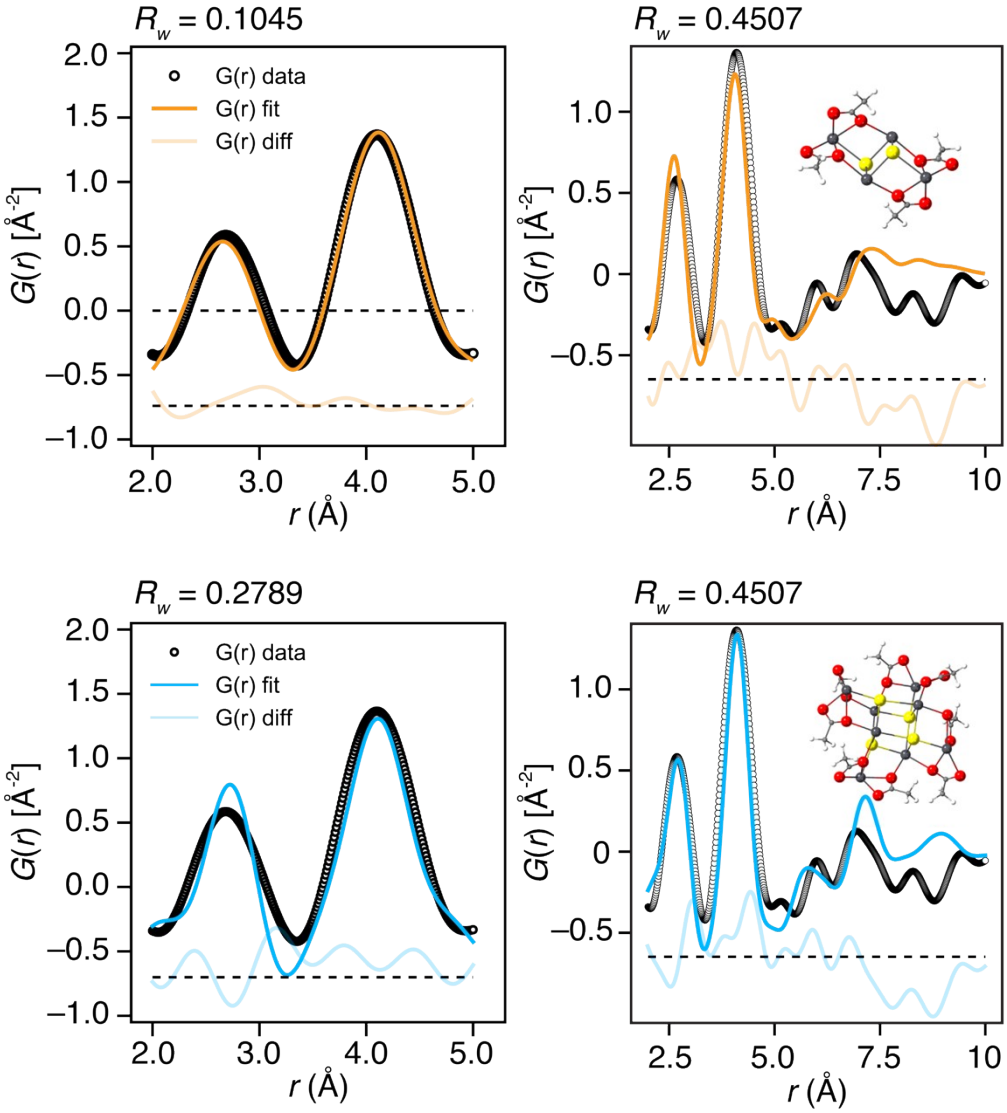

Figure S22. Fit of two candidate DFT PbS solute structures (insets) to an early-time PDF pattern collected *in situ* at 110 °C of a PbS reaction. The patterns were fit across the r = 0.2–0.5 nm (left) and r = 0.2–1.0 nm range (right).

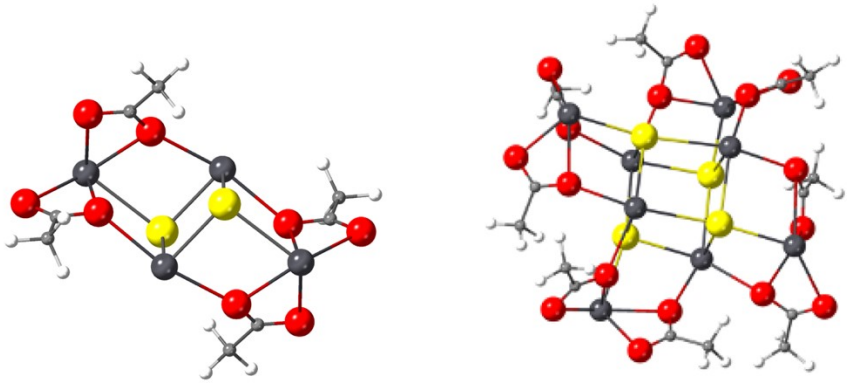

Figure S23. Candidate DFT PbS solute structures used to fit early-time PDF patterns collected *in situ* at 110 °C of a PbS reaction (atom labels: dark grey = Pb; yellow = S; red = O; light grey = C; white = hydrogen).

Section 6: Calculation of $t_{1/2,[NC]}$ / $t_{1/2,rxn}$ and its associated error

The relative duration of PbS nucleation was estimated across a range of PbS forming conditions by fitting plots of [NC] versus time to

$$[NC] = [NC]_{final}\left(1 - e^{-k_{[NC]}\left(t - t_{ind}\right)}\right) \quad (7)$$

where [NC] is the concentration of nanocrystals, $[NC]_{max}$ is the maximum concentration of PbS nanocrystals, and $k_{[NC]}$ is a rate constant (Figure S24). $k_{[NC]}$ is used as a proxy for the speed in which the [NC] increases over the course of a reaction. While not grounded in a particular rate law, we believe the closeness of fit for equation 7 justifies its usage. We converted values of $k_{[NC]}$ to $t_{1/2,[NC]}$ to approximate the absolute duration of nucleation in each PbS reaction. $t_{1/2,[NC]}$ could be determined by the half life equation for a first order reaction

$$t_{1/2,[NC]} = \frac{\ln 2}{k_{[NC]}} \quad (S5)$$

Since the absolute duration of nucleation is dependent upon the overall length of the PbS reaction, we normalize each $t_{1/2,[NC]}$ value by $t_{1/2,rxn}$, which represents the overall PbS forming reaction. Here, $t_{1/2,rxn}$ was calculated in the same manner as $t_{1/2,[NC]}$ but using the k_r value for the reaction. We approximate $t_{1/2,[NC]}$ / $t_{1/2,rxn}$ to be the fraction of total reaction time in which nuclei are added to formed in a given PbS reaction.

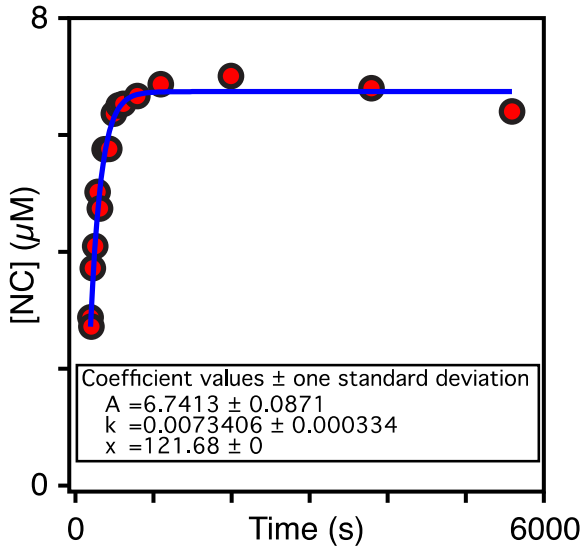

Figure S24. Fitting the temporal evolution of [NC] using equation 7 for the reaction of $Pb(oleate)_2$ and *N,N'*-4-methoxy-phenyl-dodecylthiourea at 80 °C.

Since the absolute duration of nucleation is dependent upon the overall length of the PbS reaction, we normalize each $t_{1/2,[NC]}$ value by $t_{1/2,rxn}$, which represents the overall PbS forming reaction. Here, $t_{1/2,rxn}$ was calculated in the same manner as $t_{1/2,[NC]}$ but using the k_r value for the reaction. We approximate $t_{1/2,[NC]}$ / $t_{1/2,rxn}$ to be the fraction of total reaction time in which nuclei are added to formed in a given PbS reaction. Several example fittings for the [NC] and PbS yield temporal evolution is displayed above (Figure S25). The thiourea and reaction temperature for each set of plots is shown.

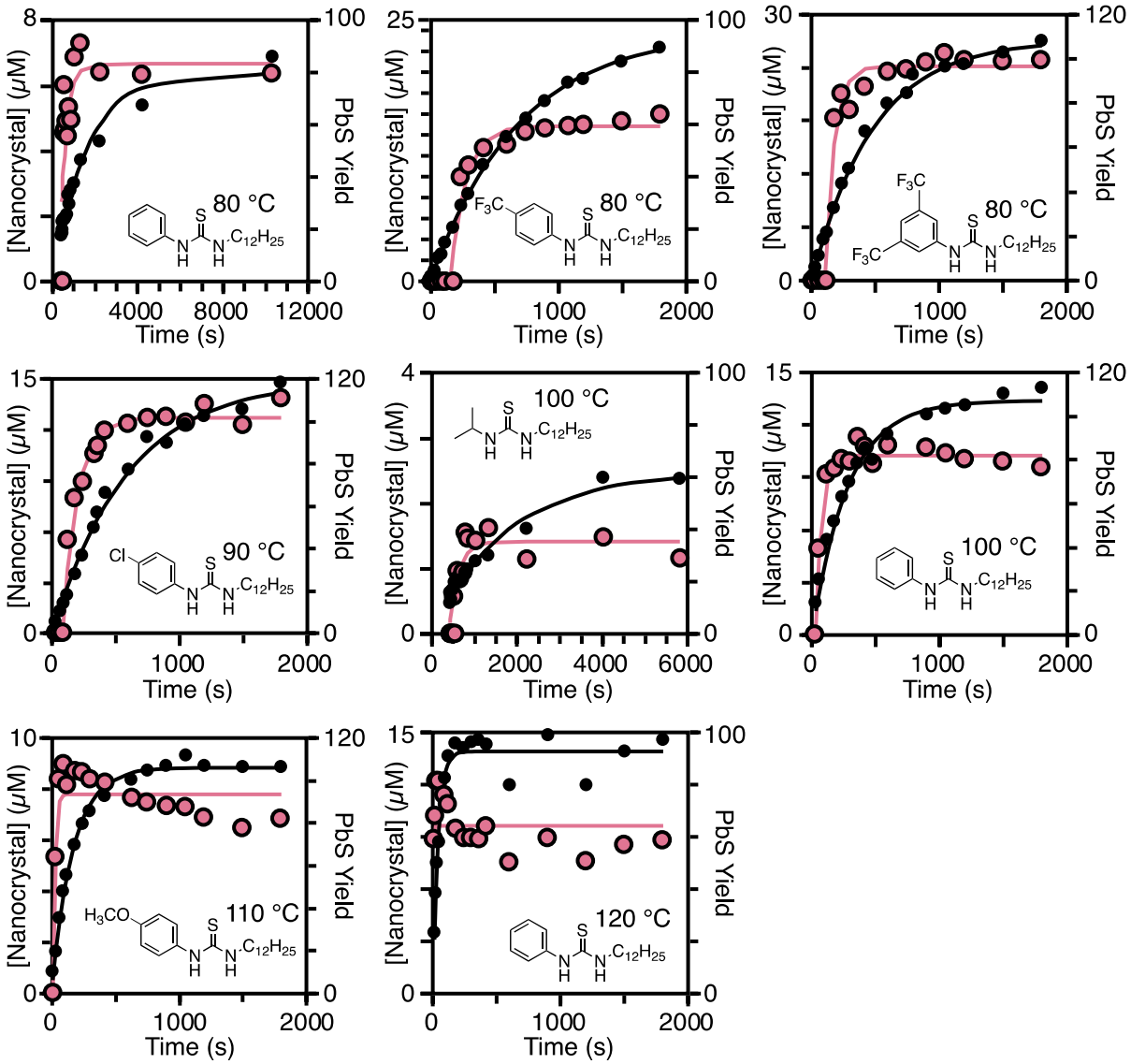

Figure S25. Fittings (solid lines) of the temporal evolution of [NC] (pink points) and PbS yield (black points) for several PbS conditions.

To estimate the uncertainty of $t_{1/2,[NC]}$ / $t_{1/2,rxn}$ we measured the relative uncertainty of both $t_{1/2,[NC]}$ and $t_{1/2,rxn}$ based on the goodness of fit to a single exponential growth function. We find that uncertainty in $t_{1/2,rxn}$ is minimal compared to $t_{1/2,[NC]}$. In general error in $t_{1/2,rxn}$ was

found to be < 5% while error in $t_{1/2,[NC]}$ ranged from < 5% to > 100% (Figure S24). The cases in which the error in $t_{1/2,[NC]}$ were largest for PbS reactions run at higher temperatures (≥ 120 °C) and with the larger final nanocrystal sizes.

For reactions > 120 °C, we do not have a quantitative estimate for $t_{1/2,[NC]}$ because equation 7 does *not* captures the overall shape of the [NC] versus time plots. However, we note that qualitatively the duration in which [NC] is increasing is shorter than the time resolution on our measurements, implying $t_{1/2,[NC]} << 5$ s. Interestingly, for the data at 110 °C and 120 °C in Figure S25, the [NC] appears to peak and then slightly decrease. We attribute the rise, then decrease in [NC] to the size-dependent extinction we used to calculate these values. Because those constants are empirically determined, variations in the peak width (*i.e.*, size distribution) may lead to variation in the determined [NC]. This will naturally be more apparent at smaller sizes where the small variations in total nanocrystal volumes can cause larger differences in nanocrystal size. That is, at smaller sizes, changes in nanocrystal volume lead to larger differences in nanocrystal diameter. Independent measurements of the [NC] using small angle X-ray scattering techniques for analogous PbS forming conditions have confirmed the monotonic increase in [NC].[13]

Section 7: Estimation of single-particle linewidths

To estimate the linewidths of the nanocrystal electronic transitions, we use a modified version of the transient spectral hole burning experiments described in Norris *et al*.[14] Similar to what we have previously reported, dynamics were checked to ensure spectral are evaluated at times much longer than carrier cooling. Briefly, features in the t = 2 ns transient absorption spectra are fit using a set of negative amplitude Gaussian function (λ = 902 and 984 nm). For larger particle sizes (λ = 1152 and 1230 nm), and additional set of a bordering positive amplitude Gaussian functions were required as well. The positive function accounts for spectral shifts associated with the excited state of the quantum dot (also known as the biexciton effect) and additional weakly allowed excited state transitions.[14-16] Representative fits for high energy excitation are shown in Figure S26. A linear baseline was used to account for the background photoinduced absorption signals. In all cases, the linewidth of the transition is taken to be the width of the negative Gaussian signal component (with variance $\sigma^2_{measured}$).

We account for the finite width of the laser pulse spectrum using by fitting it to a Gaussian lineshape (whose variance is σ^2_{laser}). Deconvolution is used to obtain the corrected linewidths (with variance of $\sigma^2_{particle}$) as a function of excitation energy:

$$\sigma^2_{measured} = \sigma^2_{laser} + \sigma^2_{particle}$$

The finite bandwidth of the laser pulse minimally affects the measured linewidth. For the sample with λ = 984 nm shown in Figure S27, the measured and deconvoluted linewidths differ by only 5%. This is a typical value for the range of samples reported here (2–7% difference). The high excitation energy ensemble linewidth is independent of the laser pulse spectrum since the spectrum is featureless and absorbs roughly equally over the excitation pulse width in that spectral region. As such, no deconvolution of the laser lineshape is used to determine the ensemble widths (extracted using the Gaussian fitting procedure described above).

The $1S_e$–$1S_h$ transition is fit to a Gaussian function on an eV scale. The resulting c (width) parameter is multiplied by the percent narrowing obtained from spectral hole burning measurements, giving the homogeneous linewidth c_0.

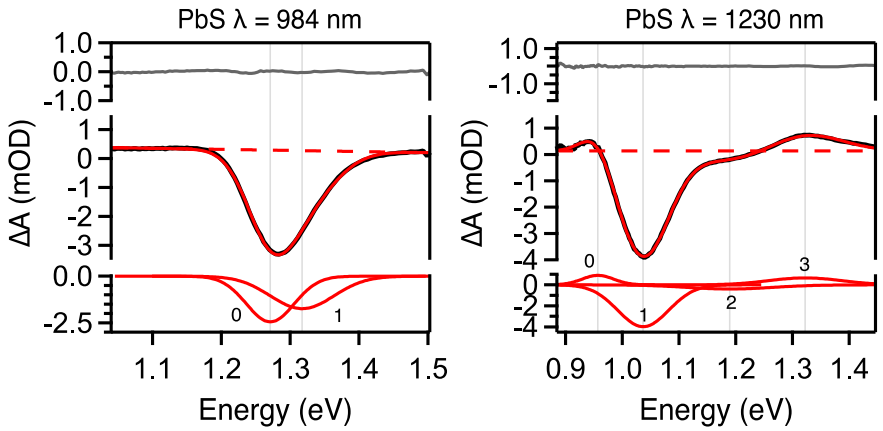

Figure S26. Example of the fit procedure used to extracted linewidths for several PbS samples described herein. The top panel (grey line) is the residual of the fit shown in the middle panel. The middle panel displays the collected data (black) and fit (red). The bottom panel shows the individual Gaussian components of the fit. A linear baseline (red dashed line) is used to account for the broad photoinduced background signal.

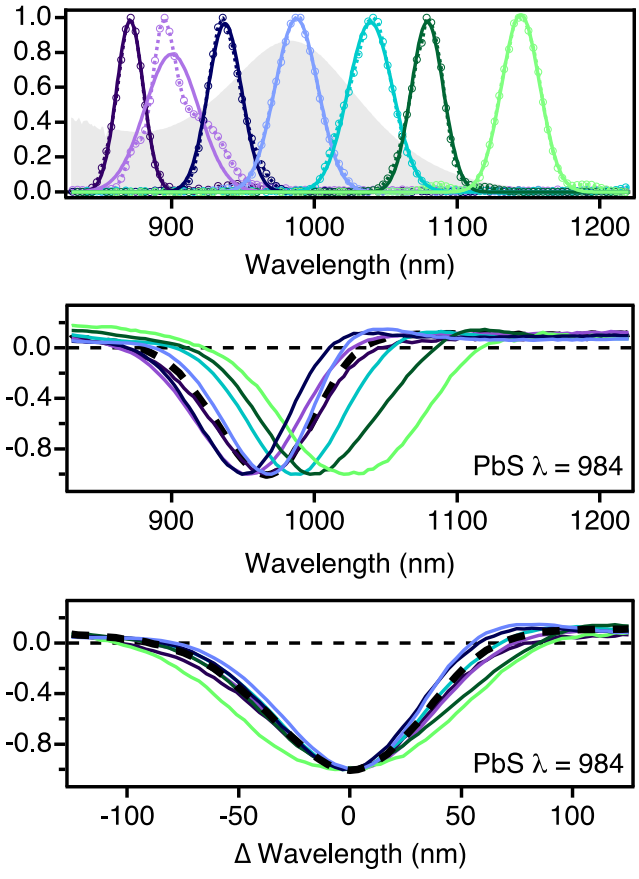

Figure S27. PbS nanocrystal extinction spectrum for a sample with $\lambda = 984$ nm along with the spectra of the laser pulses used to excitation (top). Transient spectra recorded at $t = 2$ ns as a function of wavelength (middle). Transient spectra as a function of photon wavelength that are offset to account for differences in the ground state bleach minima (bottom).

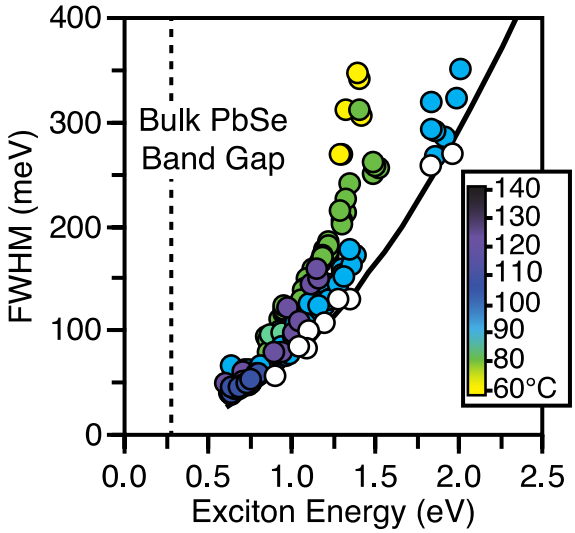

Figure S28. Final FWHM and exciton position plotted for a series of PbSe reactions run between 60–140 °C. The homogeneous linewidth for several PbSe sizes (white dots) is shown. A polynomial fit (FWHM = $A'e^{B'\lambda}$) to the homogeneous linewidth points (black line) is shown to compare with smaller final PbSe sizes.

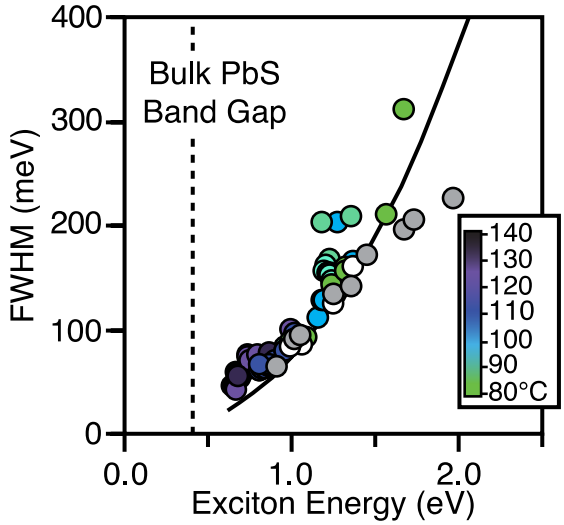

Figure S29. Final FWHM and exciton position plotted for a series of PbS reactions run between 80–140 °C. The homogeneous linewidth for several PbS sizes (white dots) is shown. A polynomial fit (FWHM = Ae^{Bx}, A = 73.8, B = 2.33, x = first excitonic transition energy) to the homogeneous linewidth points (black line) is shown to compare with smaller final PbS sizes. Data points showing the homogeneous linewidth for PbS from another method are also displayed for reference (grey dots).[17]

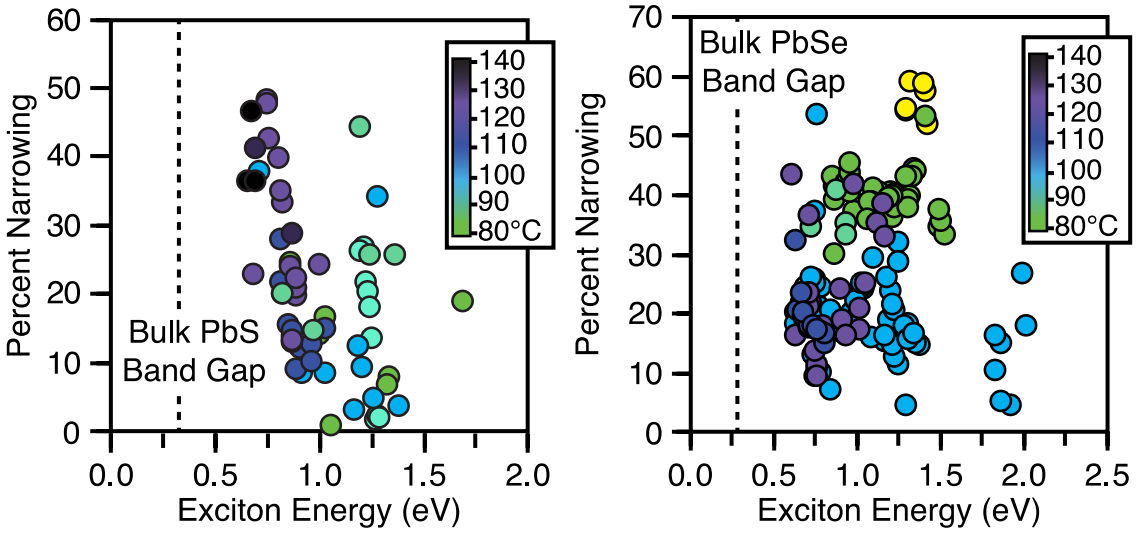

Figure S30. Plot of percent narrowing versus the position of the lowest energy excitonic transition for PbS (left) and PbSe (right). Percent narrowing describes how much narrower the intrinsic linewidth is from the observed absorbance linewidth. Percent narrowing is calculated using the same method as described previously for PbSe using the data in Figures 7B and S28–S29.[1]

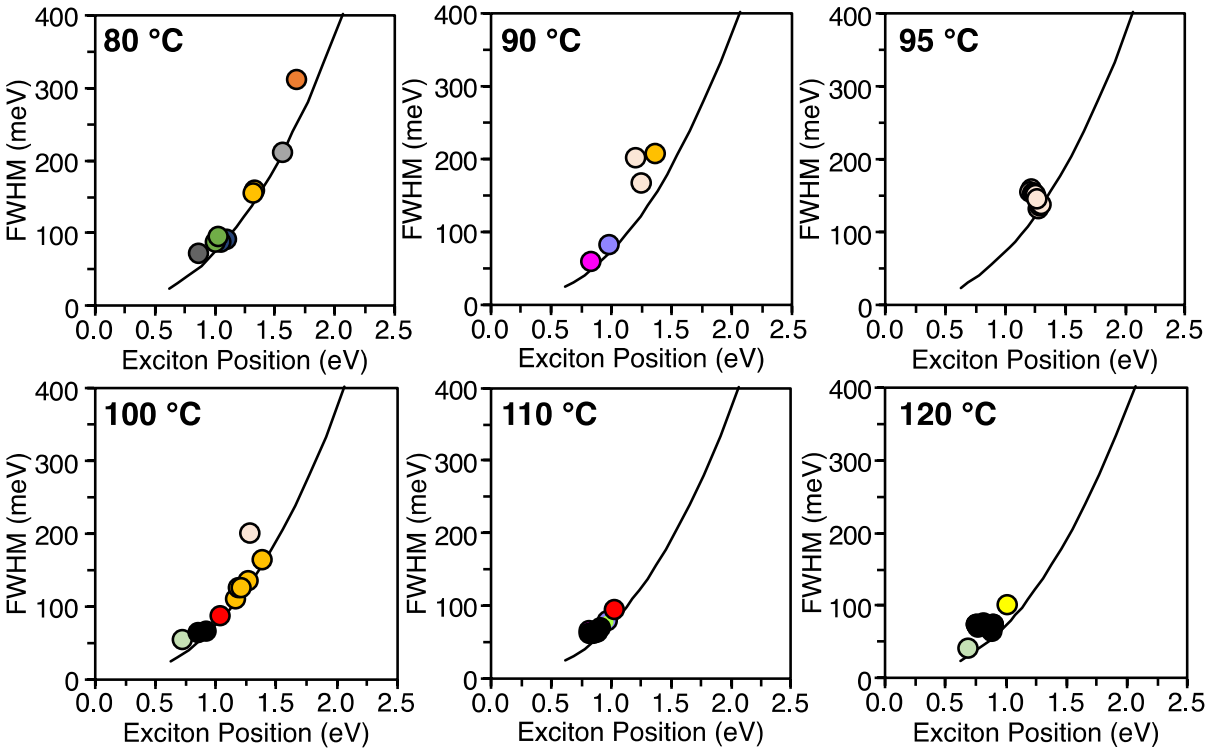

Figure S31. Final FWHM and exciton position for the PbS forming conditions shown in Figure 7B color coated based on thiourea used.

Section 8: List of *in situ* absorption experiments performed and their results

Expt #	Precursor	T (°C)	k_r (s^{-1})	t_{ind} (s)	k_{obs} (s^{-1}) (partial fit)	Q_0 (mM/s)	$[PbE]_{ind}$ (mM)	[NC] (M)
1	*TU(2-MePh,Ph)*	100	3.37E-02	7	3.80E-02	2.64E-01	2.05E+00	3.41E-06
2	*TU(3,5-$(CF_3)_2$Ph,C_{12})*	100	1.05E-02	25	1.00E-02	7.06E-02	1.95E+00	1.73E-06
3	*TU(Ph,C_{12})*	100	6.56E-04	228	9.74E-04	7.07E-03	1.74E+00	4.44E-07
4	*TU(4-CF_3Ph,C_{12})*	120	4.60E-02	3	3.83E-02	3.05E-01	1.04E+00	1.32E-06
5	*TU(4-ClPh,C_{12})*	120	2.16E-02	8	1.83E-02	1.43E-01	1.16E+00	9.20E-07
6	*TU(Ph,C_{12})*	120	1.02E-02	12	1.16E-02	9.06E-02	1.19E+00	5.97E-07
7	*TU(4-MePh,C_{12})*	120	7.35E-03	15	9.41E-03	7.33E-02	1.21E+00	6.15E-07
8	*TU(4-MeOPh,C_{12})*	120	5.30E-03	22	6.08E-03	4.78E-02	1.13E+00	4.86E-07
9	*TU(4-CF_3Ph,C_{12})*	110	2.02E-02	11	1.71E-02	1.28E-01	1.47E+00	1.38E-05
10	*TU(4-ClPh,C_{12})*	110	8.28E-03	21	8.24E-03	6.23E-02	1.44E+00	9.00E-06
11	*TU(4-MeOPh,C_{12})*	110	2.38E-03	56	3.30E-03	2.47E-02	1.51E+00	5.11E-06
12	*TU(Ph,C_{12})*	110	3.47E-03	33	4.24E-03	3.32E-02	1.17E+00	5.91E-06
13	*TU(Ph,C_{12})*	110	4.82E-03	34	5.90E-03	4.36E-02	1.60E+00	6.14E-06
14	*TU(3,5-$(CF_3)_2$Ph,C_{12})*	80	1.69E-03	182	1.67E-03	1.11E-02	2.35E+00	1.58E-05
15	*TU(4-CF_3Ph,C_{12})*	80	8.74E-04	302	8.98E-04	6.19E-03	2.10E+00	1.14E-05
16	*TU(2-MePh,Ph)*	80	1.53E-02	14	1.65E-02	1.18E-01	1.87E+00	3.66E-05
17	*TU(4-CF_3Ph,2-MePh)*	80	4.03E-02	6	4.20E-02	2.89E-01	2.12E+00	5.82E-05
18	*TU(3,5-$(CF_3)_2$Ph,2-*i*PrPh)*	80	6.89E-02	6	6.76E-02	4.11E-01	2.92E+00	6.92E-05
19	*SeU(Et_2,Cy)*	80	1.33E-02	5	1.01E-02	8.70E-02	4.24E-01	7.39E-05
20	*SeU(Et_2,Cy)*	80	9.04E-03	8	7.04E-03	5.99E-02	4.87E-01	5.77E-05
21	*SeU(Et_2,Cy)*	80	1.79E-02	3	1.58E-02	1.35E-01	4.76E-01	8.23E-05
22	*SeU(Et_2,Cy)*	80	1.08E-02	4	8.23E-03	7.17E-02	2.94E-01	8.24E-05
23	*SeU(Et_2,Cy)*	80	1.56E-02	4	1.27E-02	1.08E-01	4.84E-01	8.70E-05
24	*SeU([Et,Me],Cy)*	80	5.89E-03	8	5.16E-03	4.47E-02	3.49E-01	4.77E-05
25	*SeU([Et,Me],Cy)*	80	3.53E-03	13	2.89E-03	2.50E-02	3.33E-01	3.58E-05
26	*SeU([Et,Me],Cy)*	80	2.75E-03	16	2.57E-03	2.22E-02	3.52E-01	3.64E-05
27	*SeU(Me_2,Cy)*	80	1.30E-03	28	1.43E-03	1.24E-02	3.41E-01	9.72E-06
28	*SeU(Me_2,Cy)*	80	1.66E-03	22	1.74E-03	1.51E-02	3.33E-01	9.68E-06
29	*SeU(Me_2,Cy)*	80	1.30E-03	25	1.43E-03	1.24E-02	3.17E-01	9.79E-06
30	*SeU(Bu_2,Cy)*	80	1.42E-02	3	1.34E-02	1.15E-01	3.78E-01	1.23E-04
31	*SeU(Bu_2,Cy)*	80	1.37E-02	4	1.24E-02	1.06E-01	4.83E-01	1.16E-04
32	*SeU(Bu_2,Cy)*	80	1.09E-02	5	9.47E-03	8.12E-02	4.24E-01	1.11E-04
33	*SeU(2-MePyr,Cy)*	80	1.53E-03	29	1.50E-03	1.29E-02	3.81E-01	1.59E-05
34	*SeU(2-MePyr,Cy)*	80	2.66E-03	16	2.82E-03	2.42E-02	4.00E-01	2.10E-05
35	*SeU(2-MePyr,Cy)*	80	2.45E-03	15	2.64E-03	2.29E-02	3.48E-01	1.79E-05

36	*SeU(Pyr,Cy)*	100	3.29E-03	11	4.30E-03	3.69E-02	4.15E-01	6.95E-06
37	*SeU(Pyr,Cy)*	100	3.18E-03	11	3.86E-03	3.32E-02	3.85E-01	6.86E-06
38	*SeU(Pyr,Cy)*	100	3.28E-03	11	4.17E-03	3.59E-02	3.96E-01	6.99E-06
39	*SeU([4-MeOPh,Me],Bu)*	110	2.38E-03	10	3.21E-03	2.80E-02	2.81E-01	4.42E-06
40	*SeU([4-MeOPh,Me],Cy)*	110	4.53E-03	7	5.53E-03	4.79E-02	3.45E-01	7.72E-06
41	*SeU([4-MeOPh,Me],Cy)*	110	1.61E-03	12	1.89E-03	1.67E-02	2.00E-01	3.06E-06
42	*SeU([4-MeOPh,Me],Cy)*	110	2.22E-03	10	2.62E-03	2.30E-02	2.19E-01	4.24E-06
43	*SeU(Me_2,Cy)*	90	4.52E-03	13	4.32E-03	3.67E-02	4.96E-01	1.55E-05
44	*SeU(Me_2,Cy)*	90	2.71E-03	20	2.60E-03	2.22E-02	4.49E-01	1.02E-05
45	*SeU(Me_2,Cy)*	90	4.23E-03	11	4.10E-03	3.52E-02	4.12E-01	1.60E-05
46	*SeU(Pyr,Cy)*	90	6.74E-04	47	9.09E-04	7.84E-03	3.77E-01	3.46E-06
47	*SeU(Pyr,Cy)*	90	7.24E-04	44	9.67E-04	8.34E-03	3.72E-01	4.27E-06
48	*SeU($Allyl_2$,Cy)*	80	1.66E-03	18	1.74E-03	1.52E-02	2.73E-01	3.06E-05
49	*SeU($Allyl_2$,Cy)*	80	1.82E-03	18	1.94E-03	1.69E-02	2.95E-01	3.06E-05
50	*SeU($Allyl_2$,Cy)*	80	1.03E-03	27	1.17E-03	1.03E-02	2.72E-01	2.67E-05
51	*SeU(Pyr,Bu)*	110	4.20E-03	8	4.56E-03	3.96E-02	3.14E-01	3.33E-06
52	*SeU(Pyr,Bu)*	110	4.13E-03	9	4.40E-03	3.82E-02	3.30E-01	3.56E-06
53	*SeU(Pyr,Bu)*	120	1.09E-02	3	1.11E-02	9.69E-02	2.57E-01	4.00E-06
54	*SeU(Pyr,Cy)*	110	8.68E-03	5	9.31E-03	8.03E-02	3.74E-01	8.62E-06
55	*SeU(Pyr,Cy)*	110	3.45E-03	8	3.41E-03	2.98E-02	2.45E-01	4.63E-06
56	*SeU(Pyr,Cy)*	110	5.12E-03	7	5.39E-03	4.67E-02	3.32E-01	5.54E-06
57	*SeU([4-MeOPh,Me],Bu)*	120	2.78E-03	3	2.78E-03	2.48E-02	8.04E-02	2.61E-06
58	*SeU(Pyr,Bu)*	120	6.31E-03	4	7.04E-03	6.16E-02	2.54E-01	2.09E-06
59	*SeU([4-MeOPh,Me],Cy)*	120	7.76E-03	3	8.55E-03	7.48E-02	2.57E-01	6.04E-06
60	*SeU([4-MeOPh,Me],Cy)*	120	6.74E-03	3	7.08E-03	6.22E-02	2.09E-01	5.36E-06
61	*SeU([4-MeOPh,Me],Cy)*	120	8.56E-03	3	8.64E-03	7.59E-02	2.15E-01	6.33E-06
62	*SeU([Ph,Me],Cy)*	120	7.46E-03	3	8.41E-03	7.39E-02	2.10E-01	6.11E-06
63	*SeU([Ph,Me],Cy)*	120	4.70E-03	3	5.55E-03	4.92E-02	1.29E-01	4.29E-06
64	*SeU([Ph,Me],Cy)*	120	4.70E-03	2	5.13E-03	4.56E-02	1.05E-01	4.51E-06
65	*SeU([4-ClPh,Me],Cy)*	120	4.58E-03	3	5.82E-03	5.15E-02	1.62E-01	4.26E-06
66	*SeU([4-ClPh,Me],Cy)*	120	6.10E-03	3	8.31E-03	7.30E-02	2.09E-01	5.48E-06
67	*SeU([4-ClPh,Me],Cy)*	120	5.05E-03	3	6.59E-03	5.80E-02	1.93E-01	4.97E-06
68	*SeU(Pip,Cy)*	80	2.41E-02	2	2.23E-02	1.94E-01	3.37E-01	1.39E-04
69	*SeU(Bu_3)*	80	7.17E-03	6	6.70E-03	5.80E-02	3.50E-01	7.21E-05

70	*SeU(Bu_3)*	80	7.83E-03	6	7.00E-03	6.05E-02	3.61E-01	6.84E-05
71	*SeU(Bu_3)*	80	9.18E-03	5	9.08E-03	7.84E-02	3.67E-01	6.83E-05
72	*SeU([Bu,Me],Bu)*	80	2.16E-03	17	2.19E-03	1.90E-02	3.15E-01	2.00E-05
73	*SeU([Bu,Me],Bu)*	80	2.66E-03	14	2.78E-03	2.41E-02	3.34E-01	1.92E-05
74	*SeU([Bu,Me],Bu)*	80	2.09E-03	17	2.29E-03	1.98E-02	3.38E-01	1.77E-05
75	*SeU($Allyl_2$,Bu)*	80	4.03E-03	10	3.77E-03	3.27E-02	3.27E-01	1.29E-05

Section 9: *In situ* absorption data and fittings

As described in the experimental section the data were fit in two ways. Here we present the raw data from the dip probe experiments (λ = 400 nm) and (i) the overall fit to a single exponential and (ii) the second fit, designed to carefully capture the induction delay and the critical monomer concentration.

Expt. 1

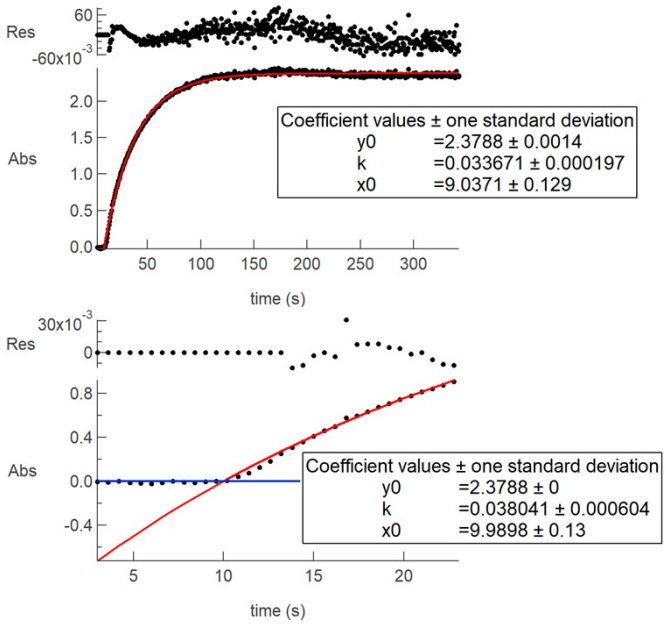

Expt. 2

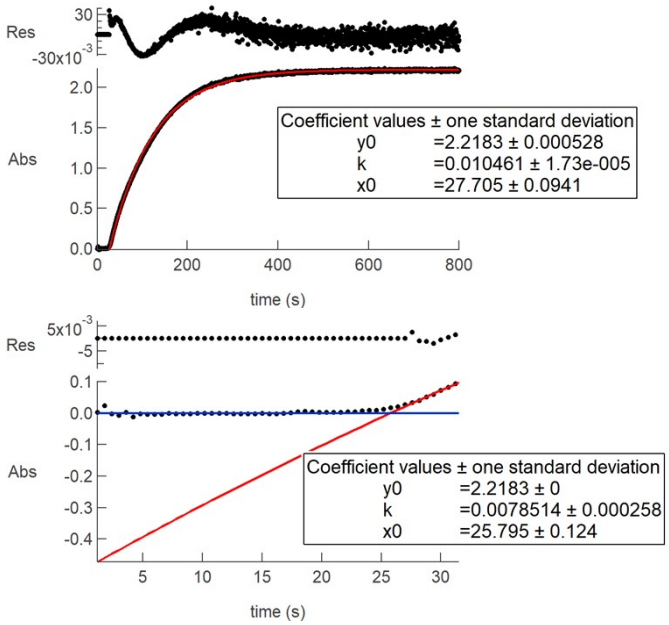

Expt. 3

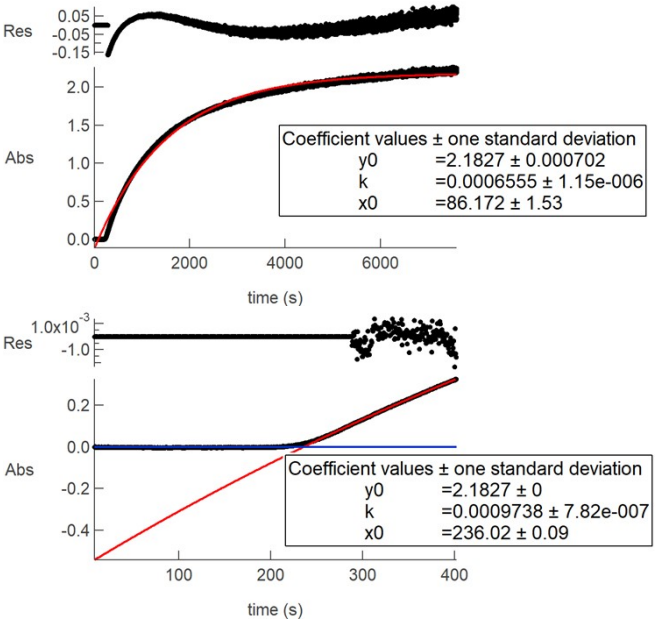

Expt. 4

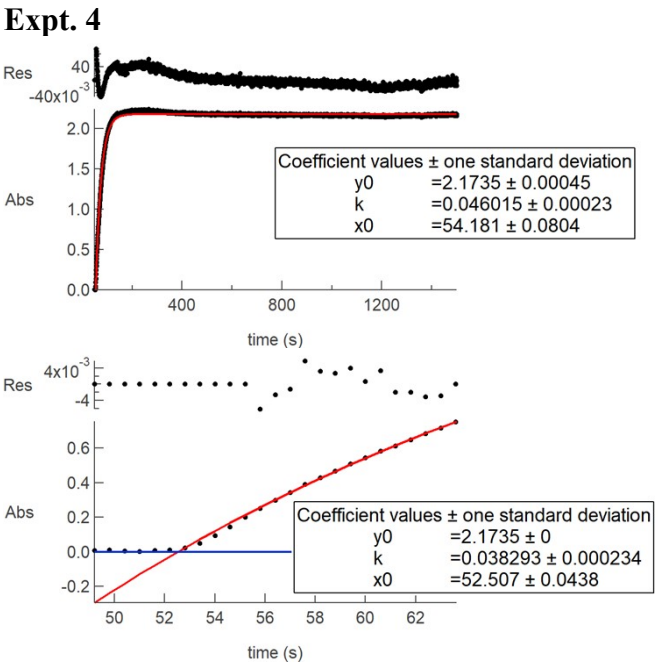

Expt. 5

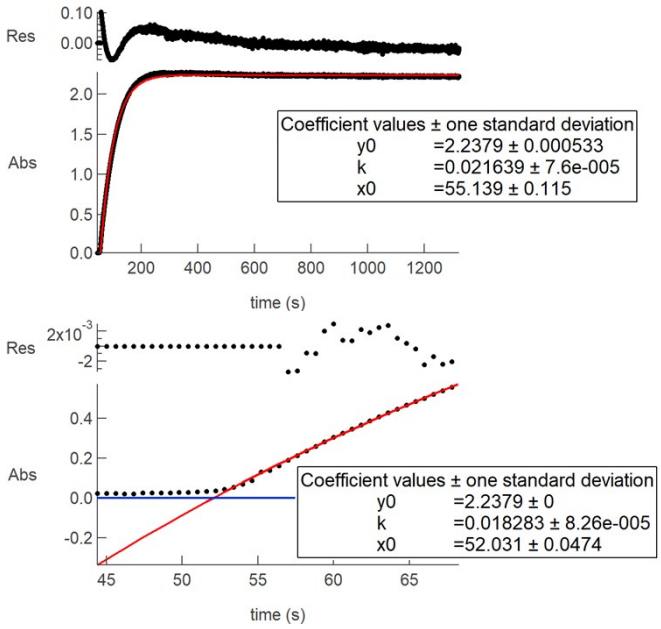

Expt. 6

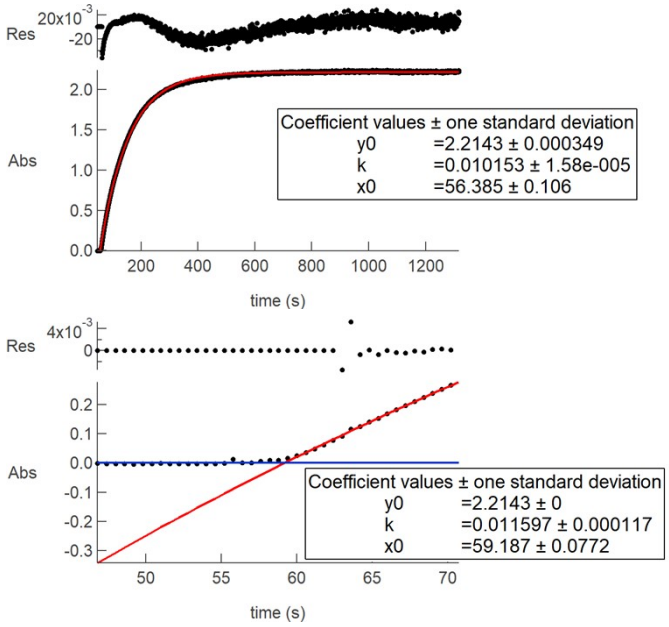

Expt. 7

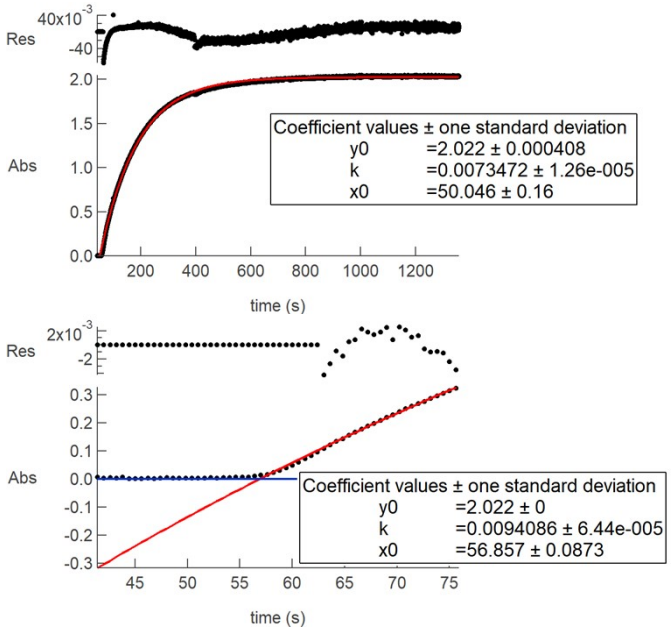

Expt. 8

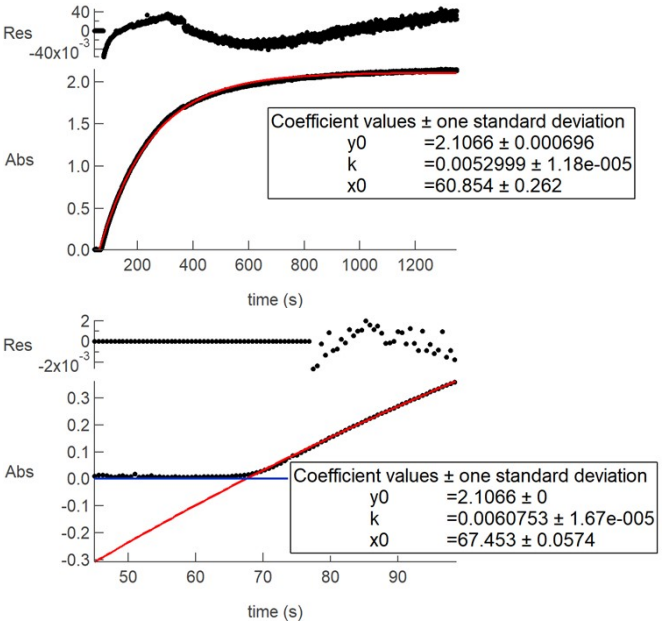

Expt. 9

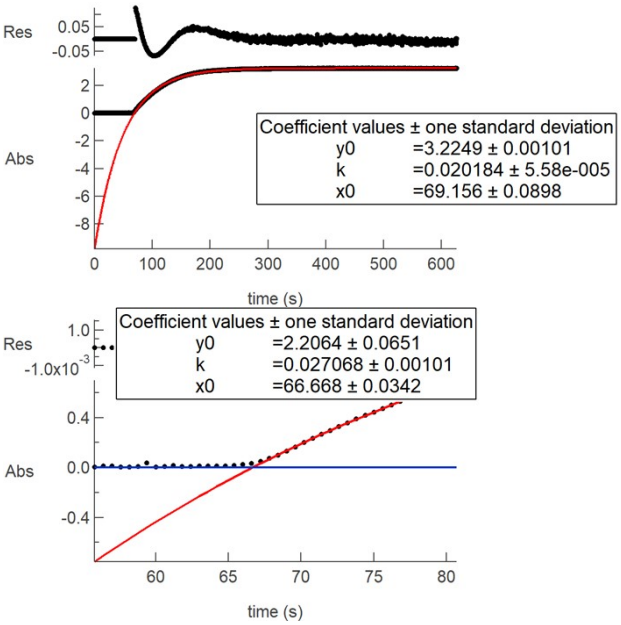

Expt. 10

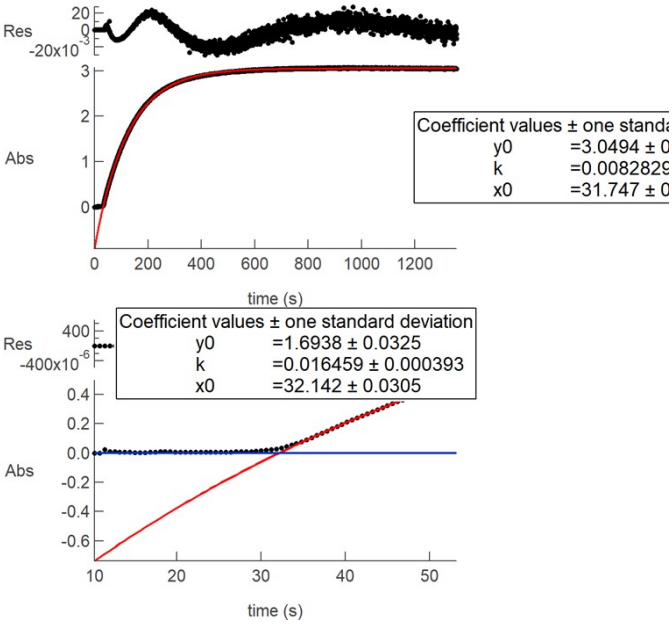

Expt. 11

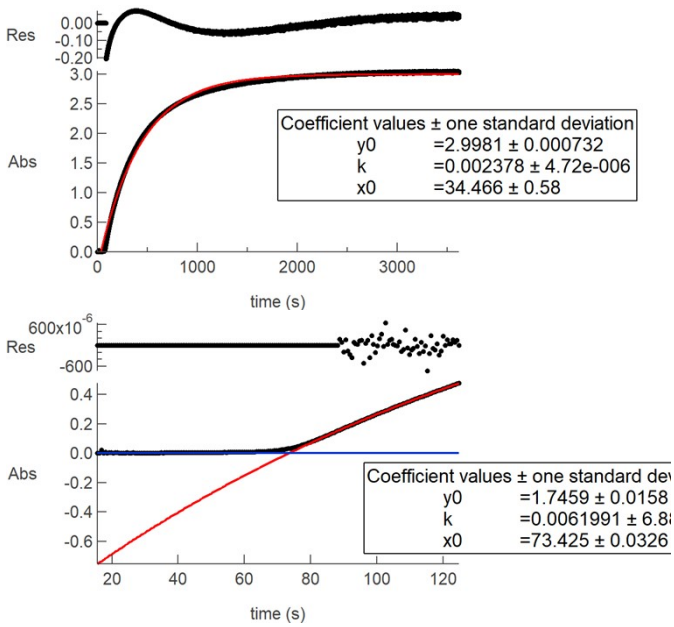

Expt. 12

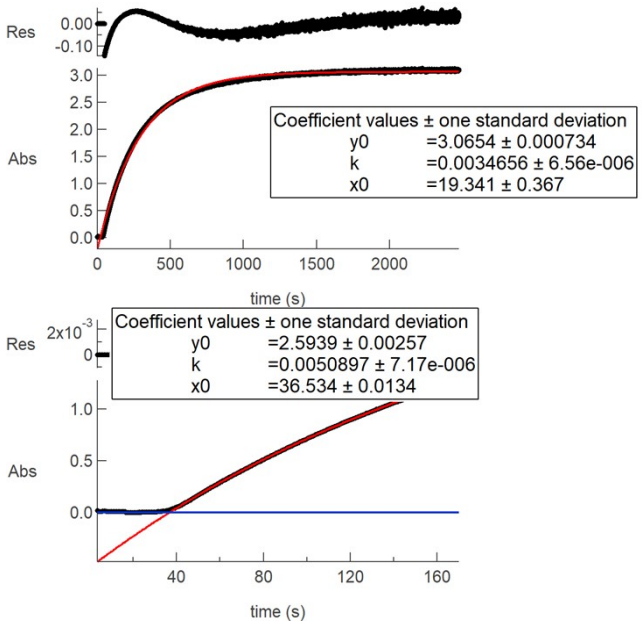

Expt. 13

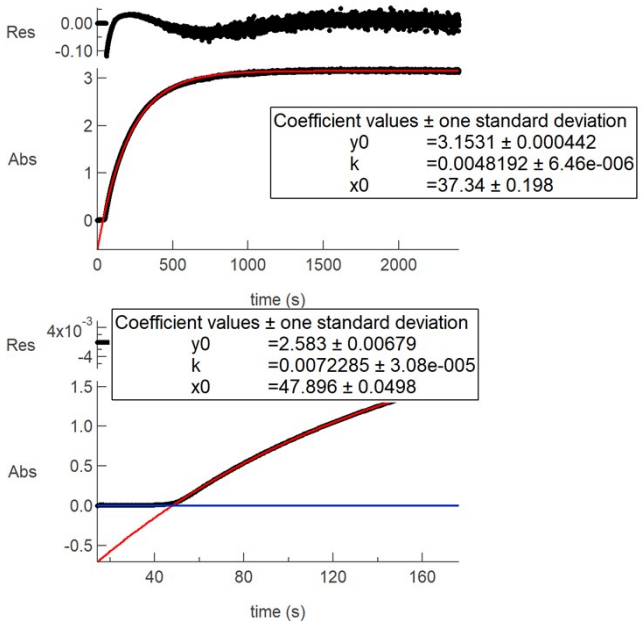

Expt. 14

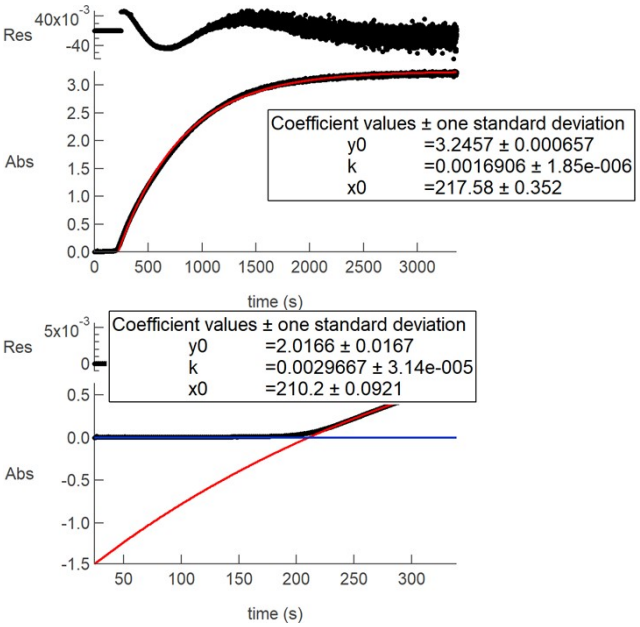

Expt. 15

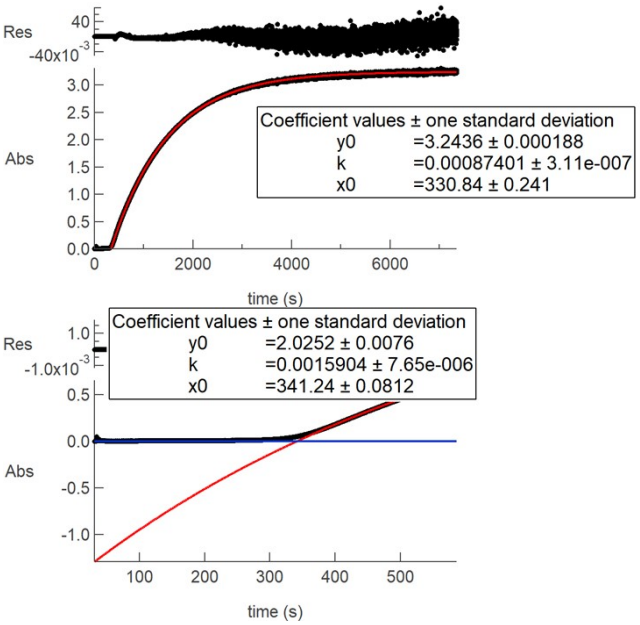

Expt. 16

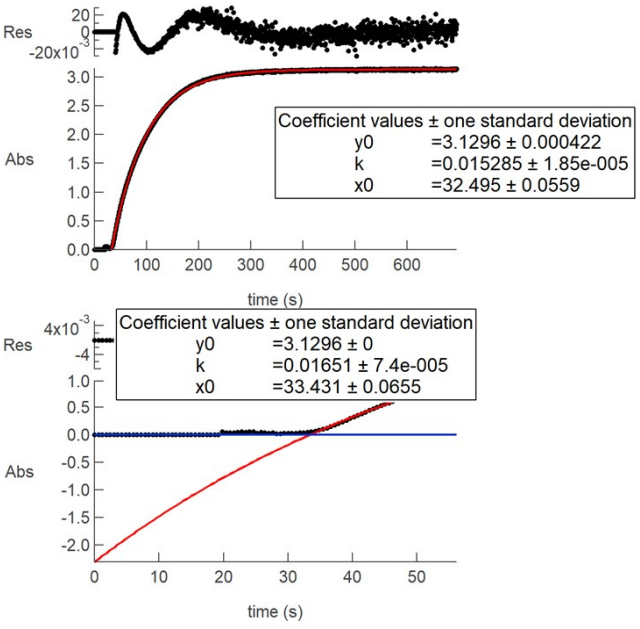

Expt. 17

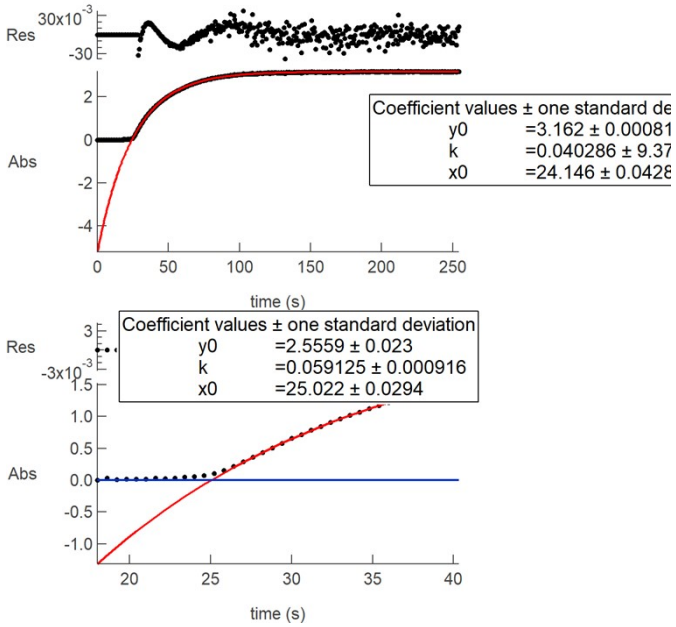

Expt. 18

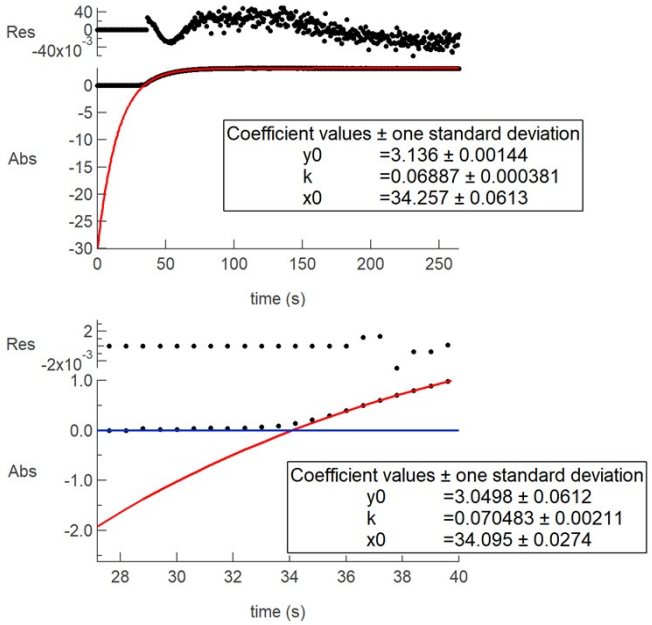

Expt. 19

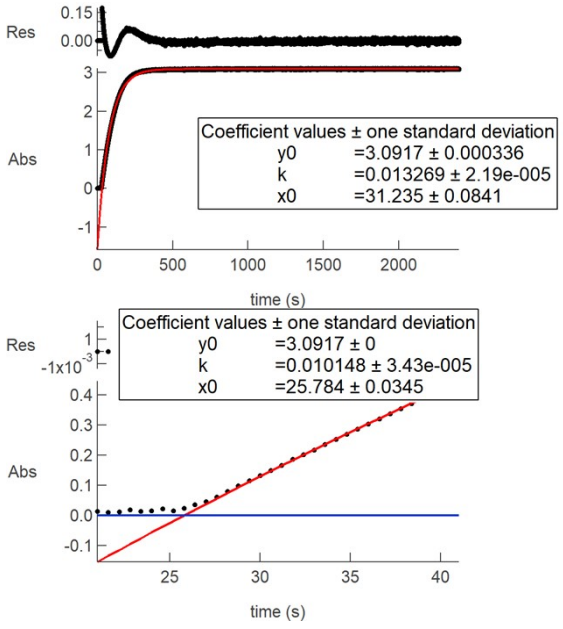

Expt. 20

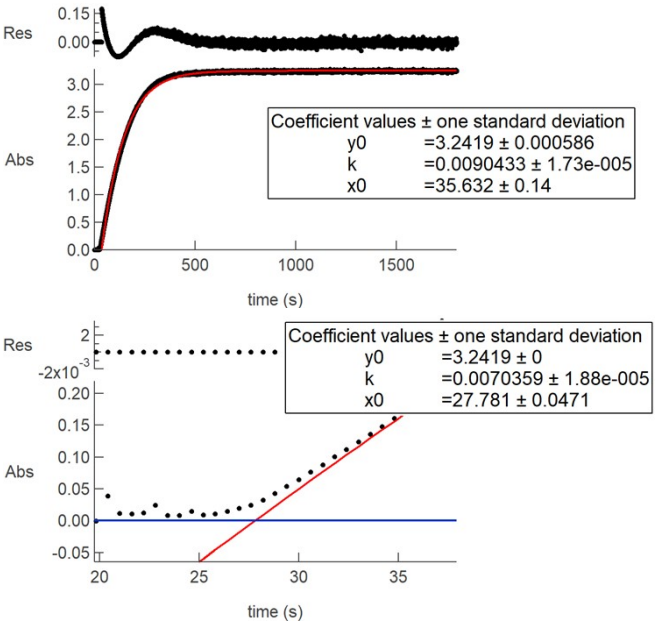

Expt. 21

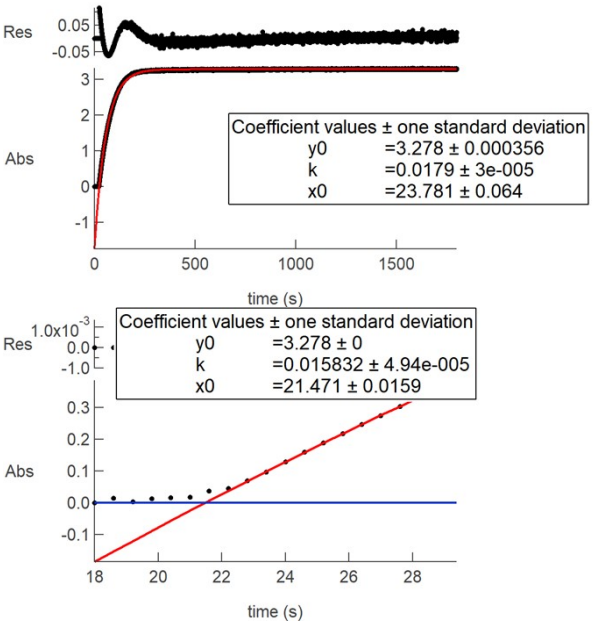

Expt. 22

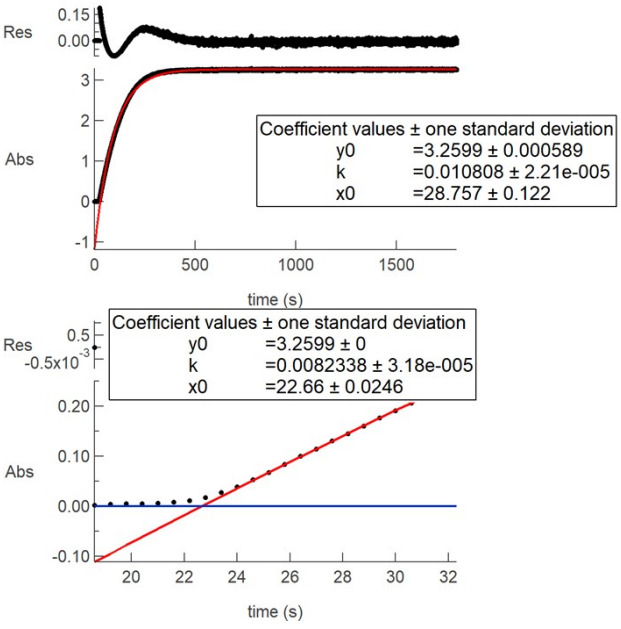

Expt. 23

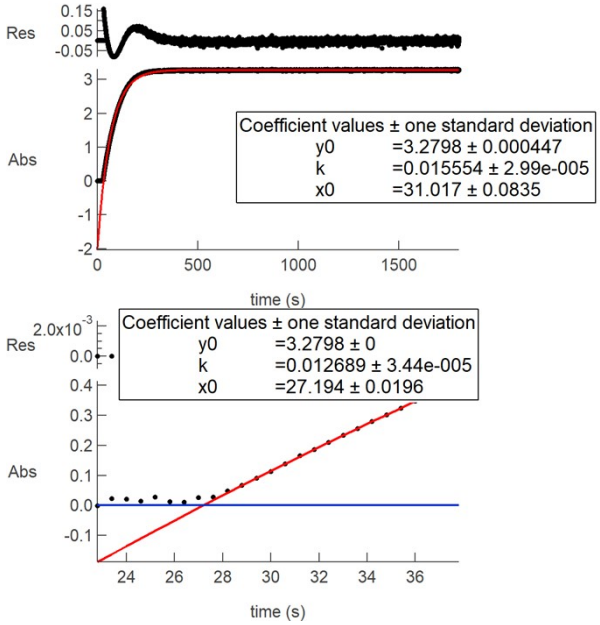

Expt. 24

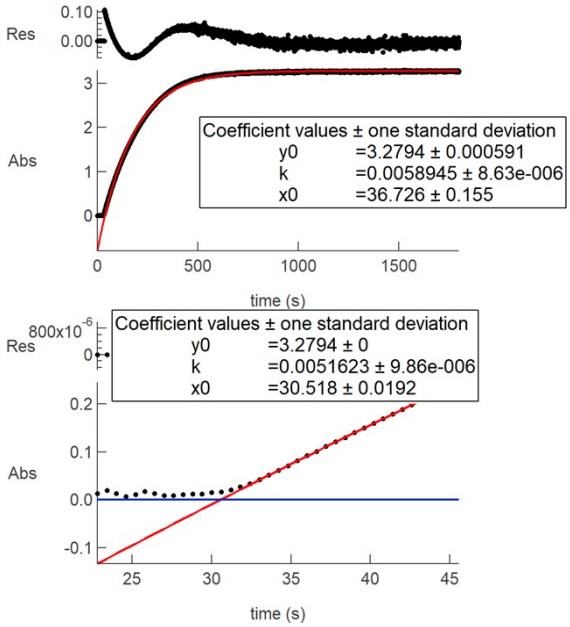

Expt. 25

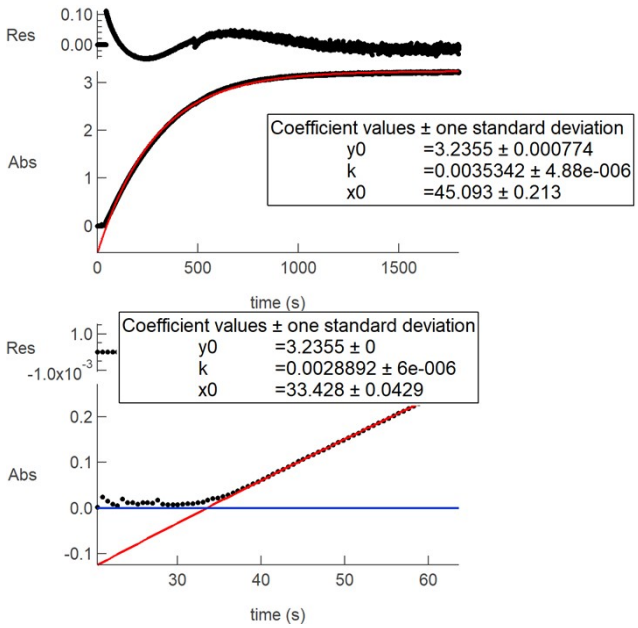

Expt. 26

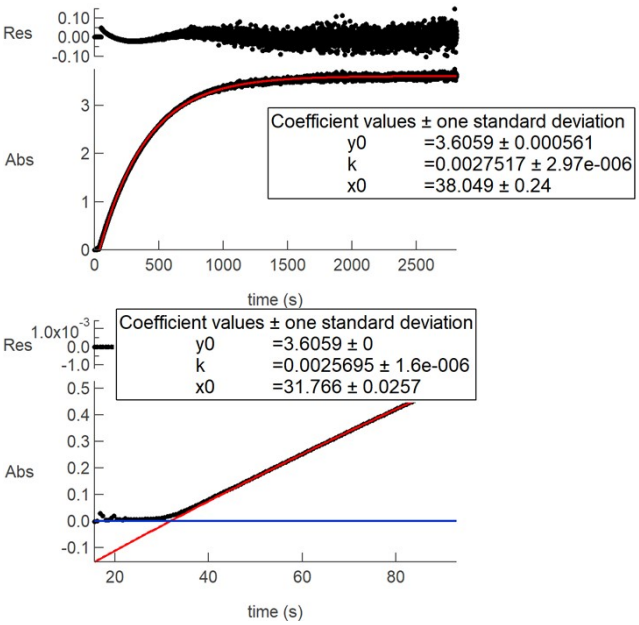

Expt. 27

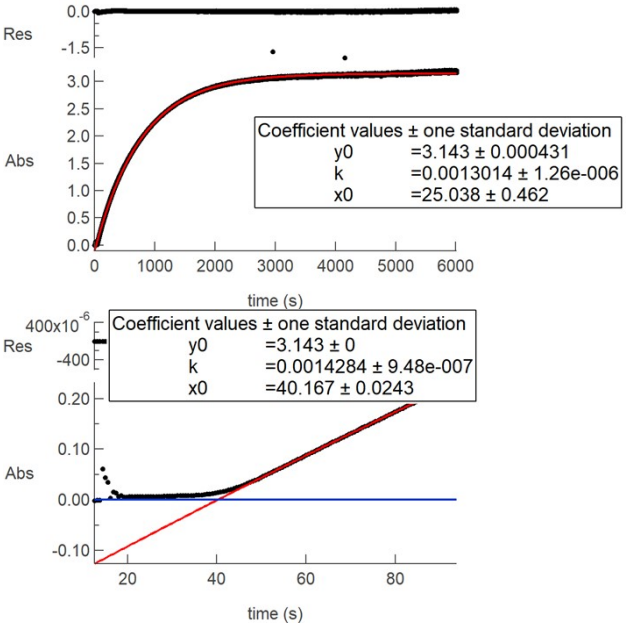

Expt. 28

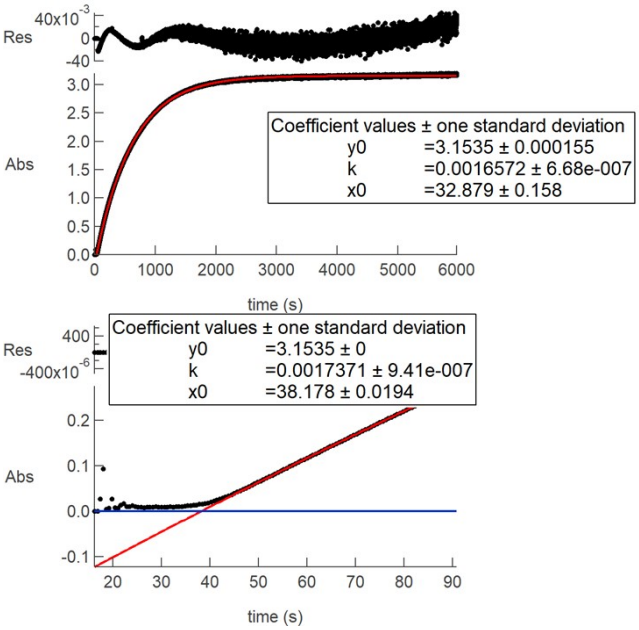

Expt. 29

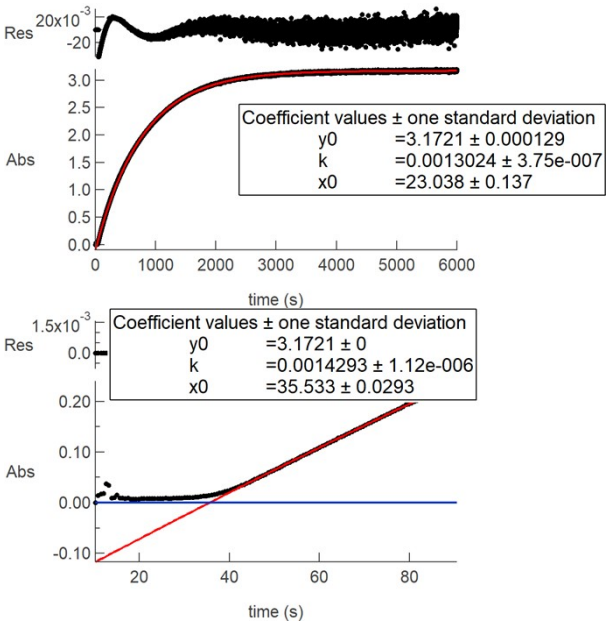

Expt. 30

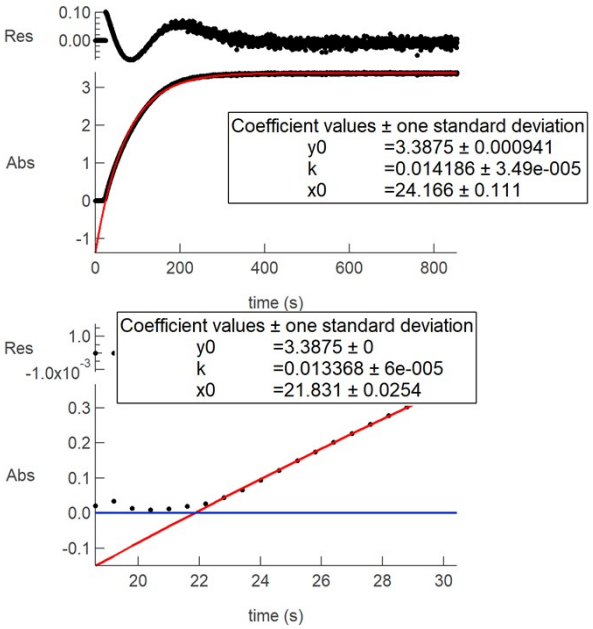

Expt. 31

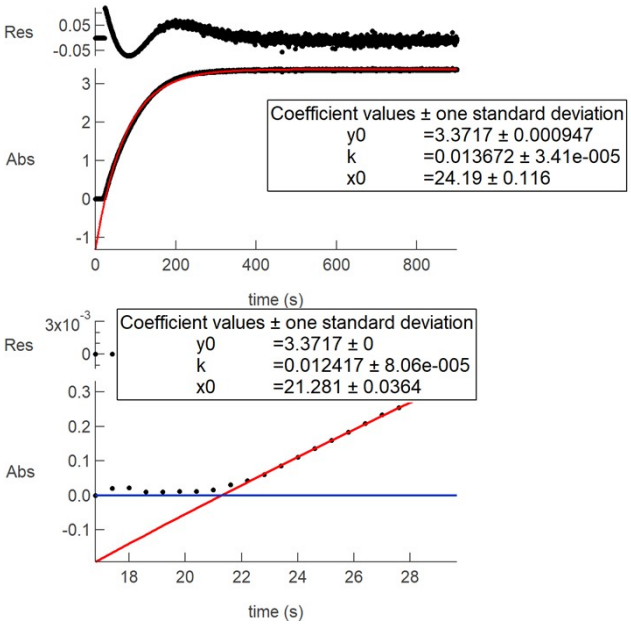

Expt. 32

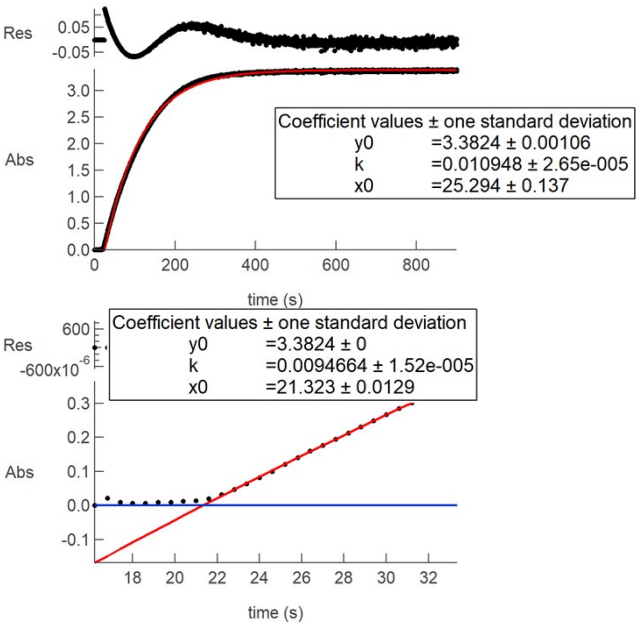

Expt. 33

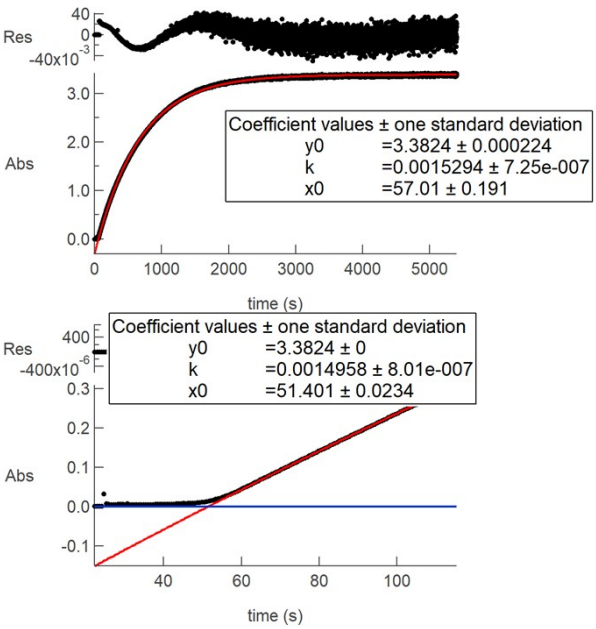

Expt. 34

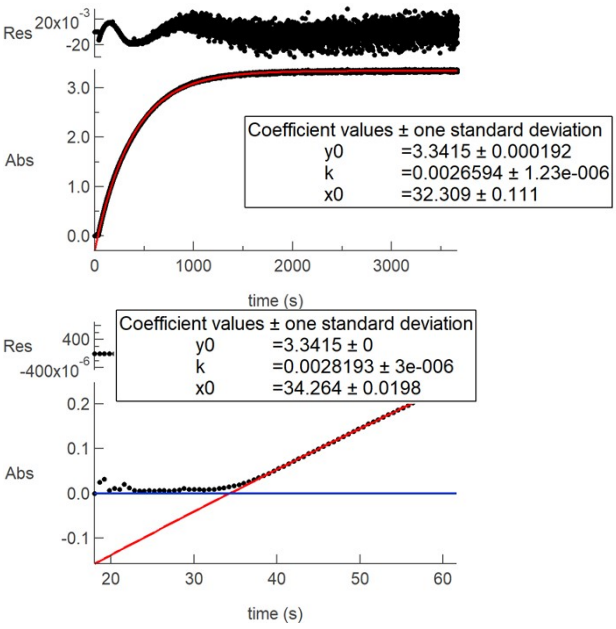

Expt. 35

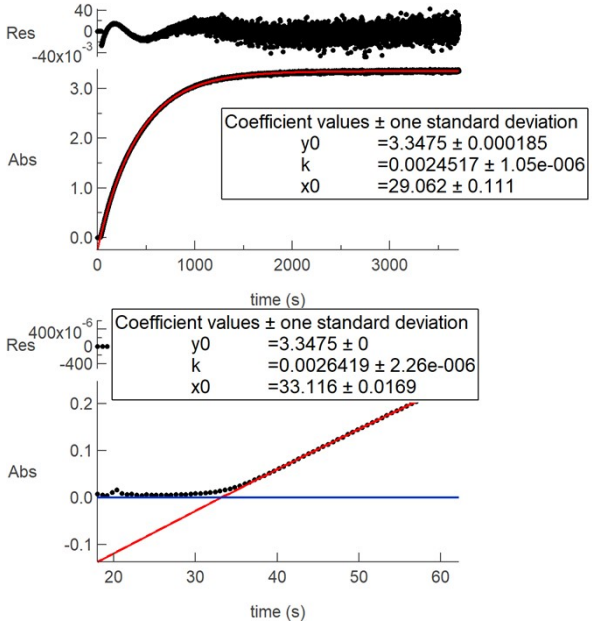

Expt. 36

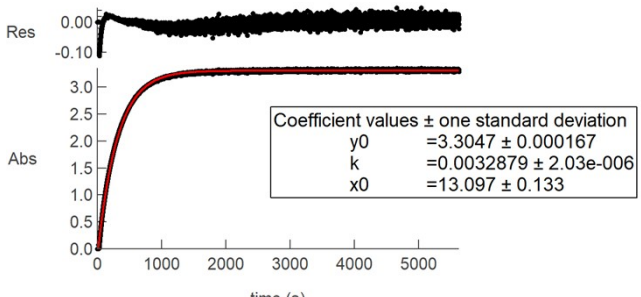

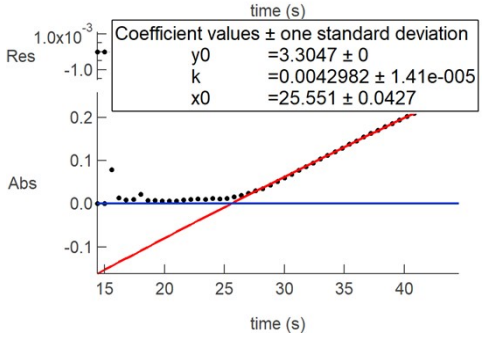

Expt. 37

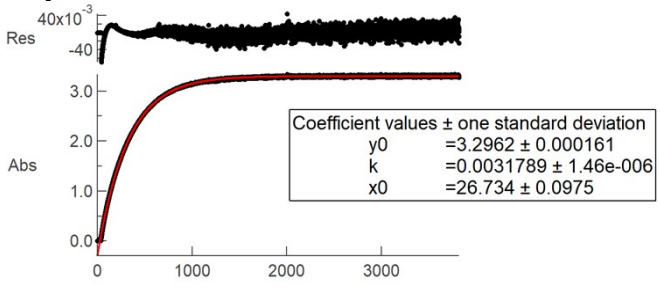

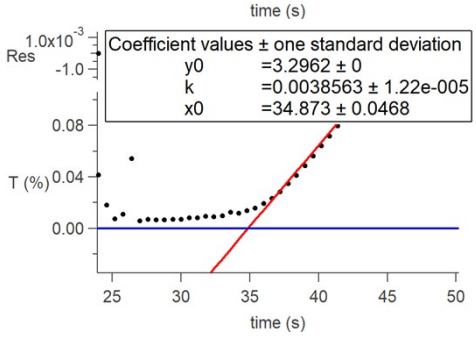

Expt. 38

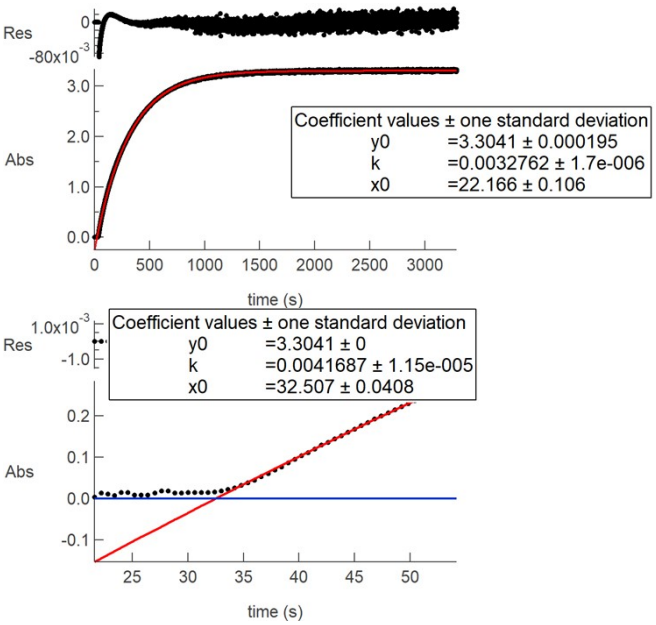

Expt. 39

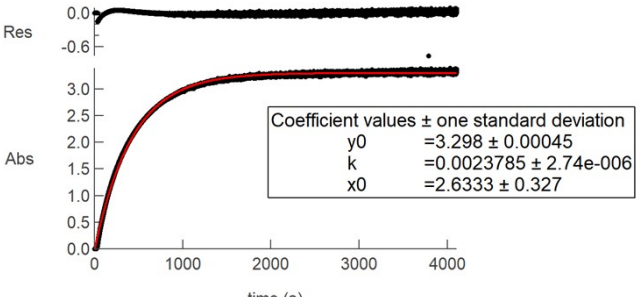

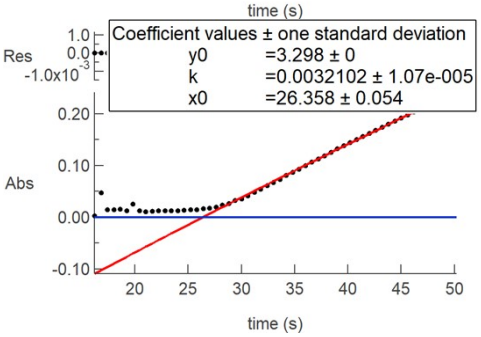

Expt. 40

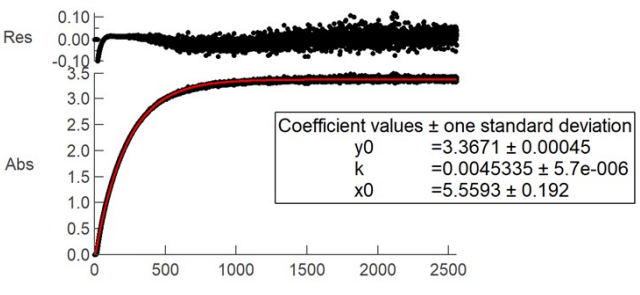

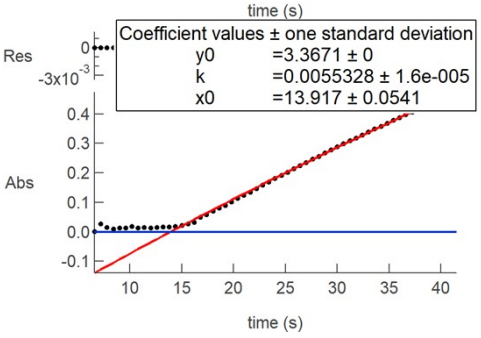

Expt. 41

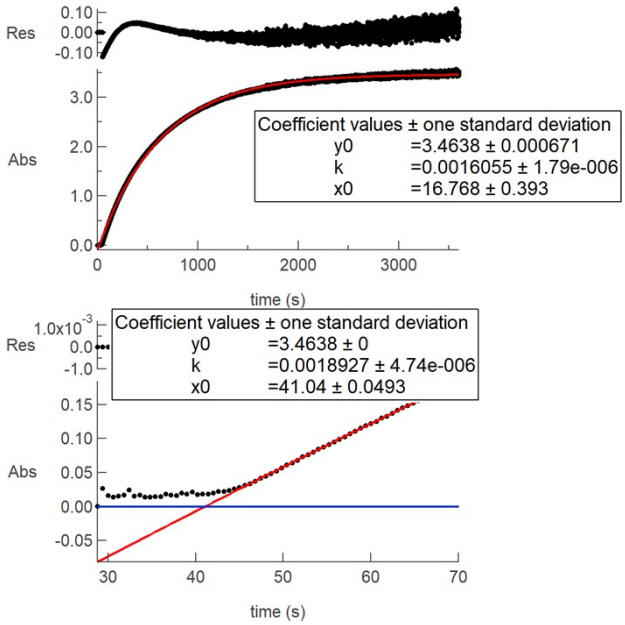

Expt. 42

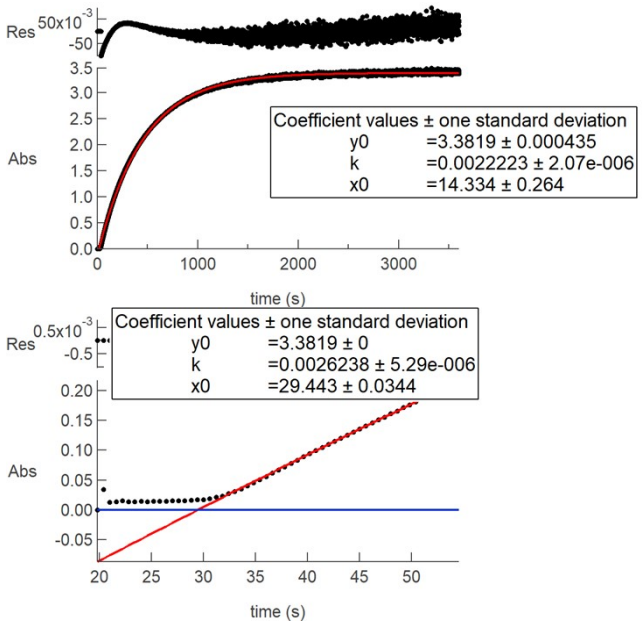

Expt. 43

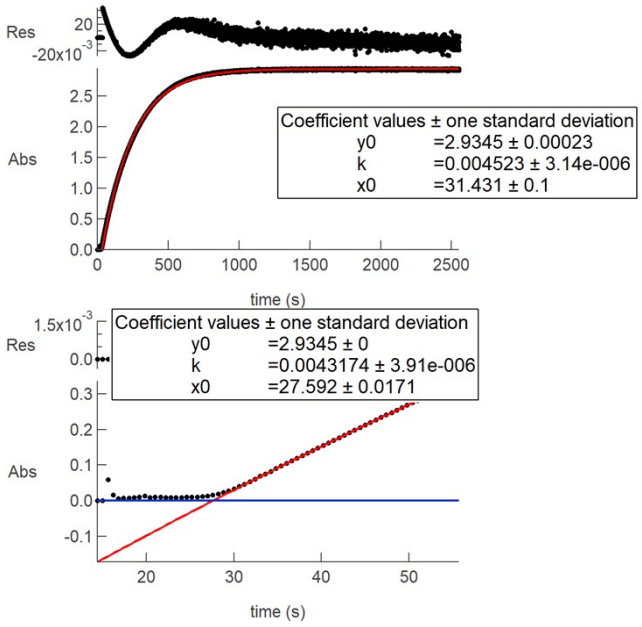

Expt. 44

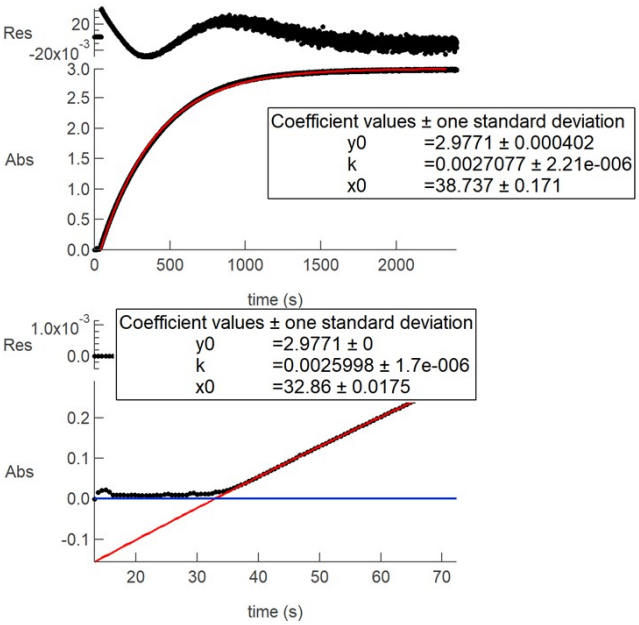

Expt. 45

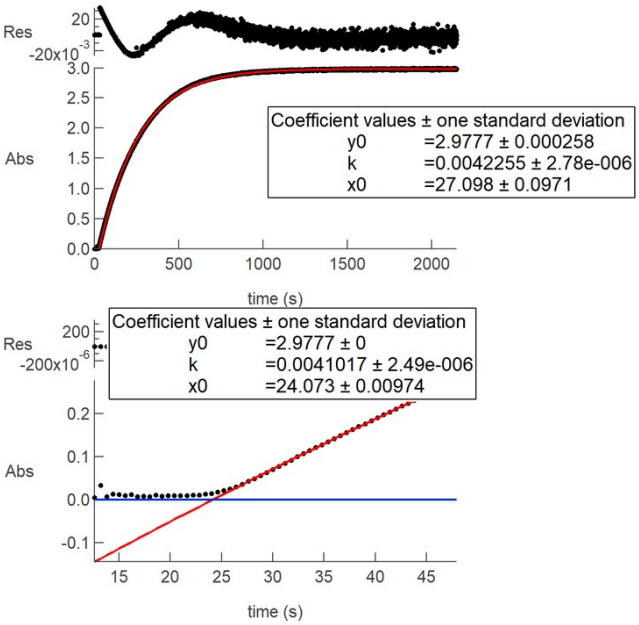

Expt. 46

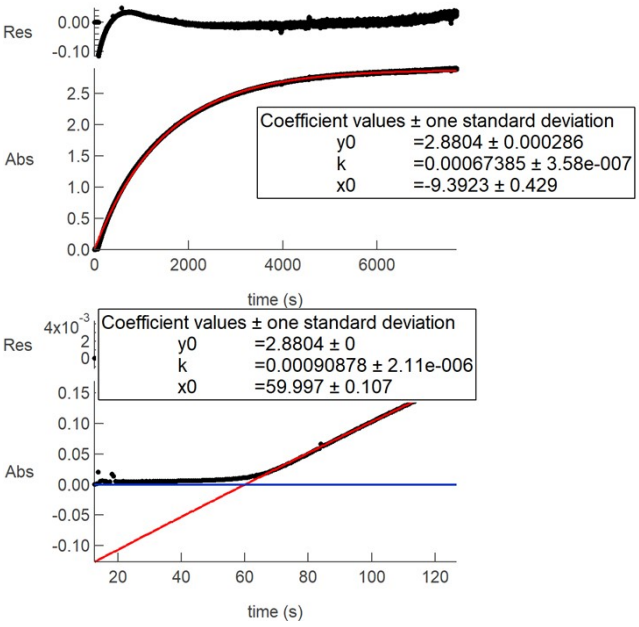

Expt. 47

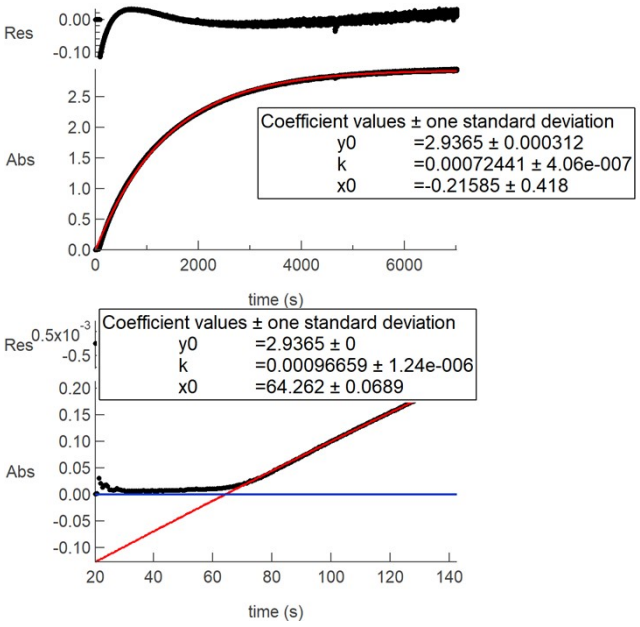

Expt. 48

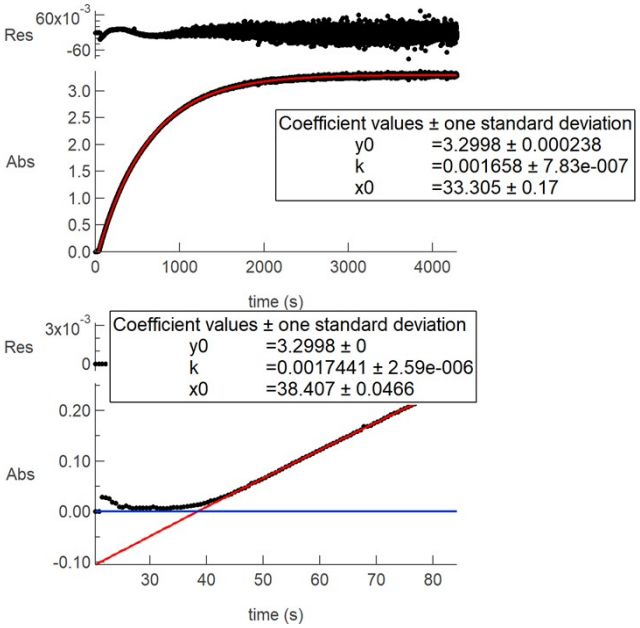

Expt. 49

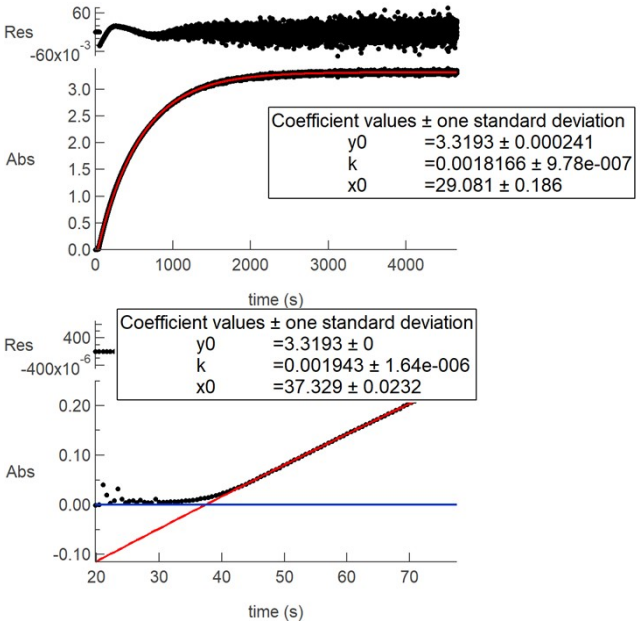

Expt. 50

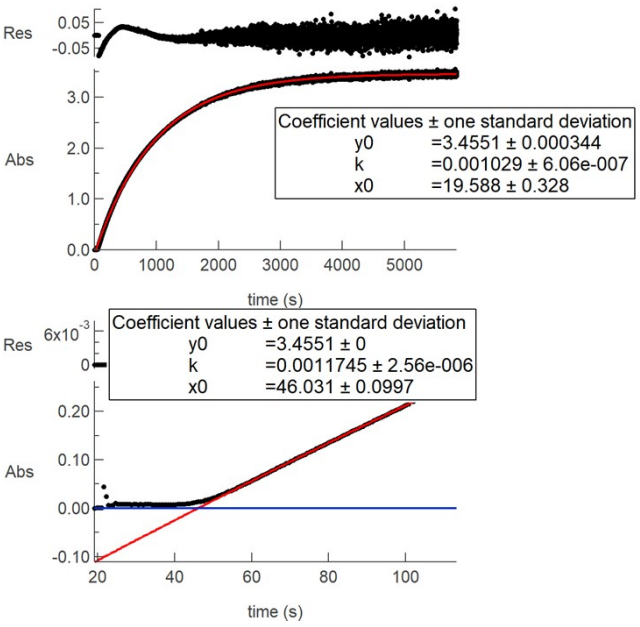

Expt. 51

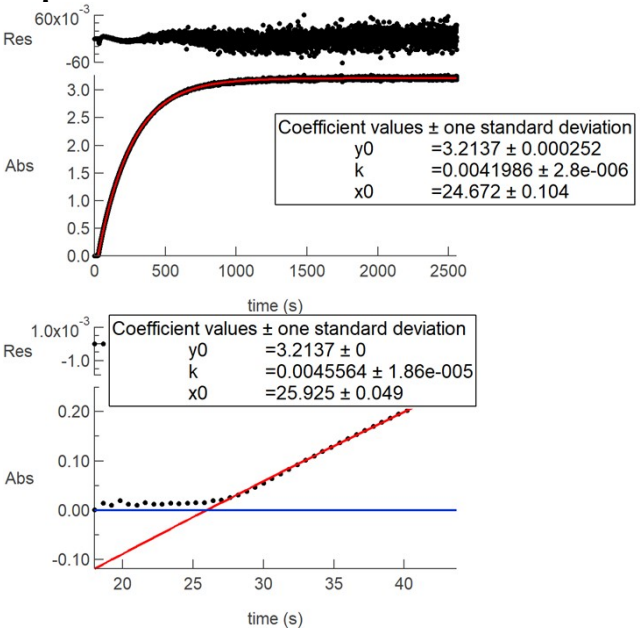

Expt. 52

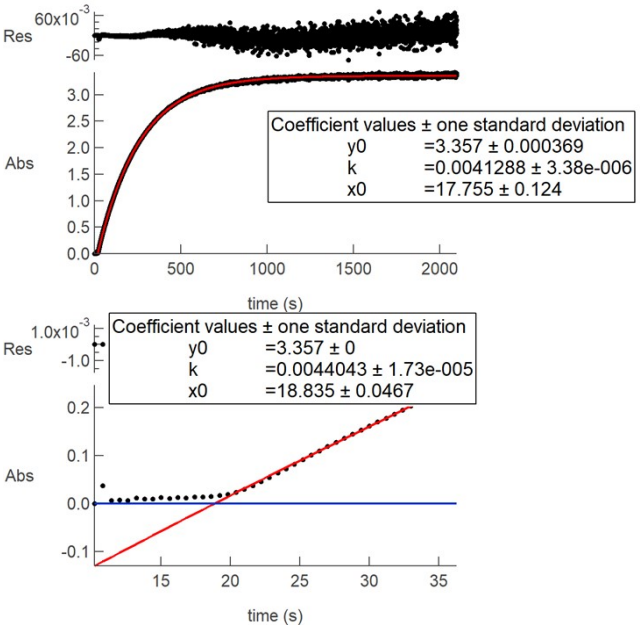

Expt. 53

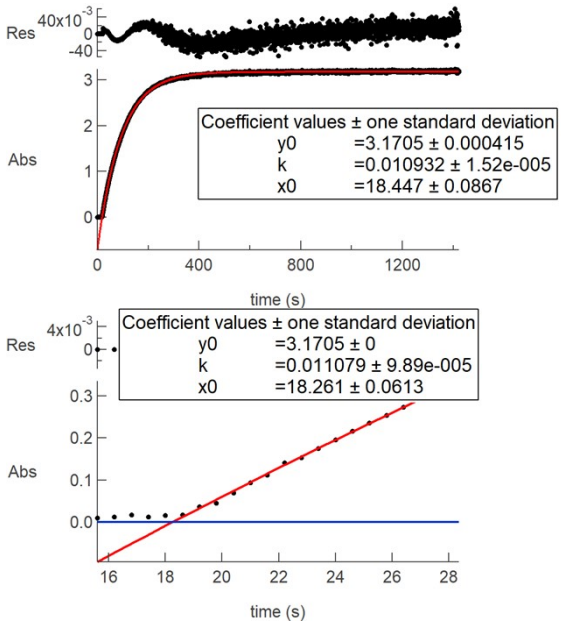

Expt. 54

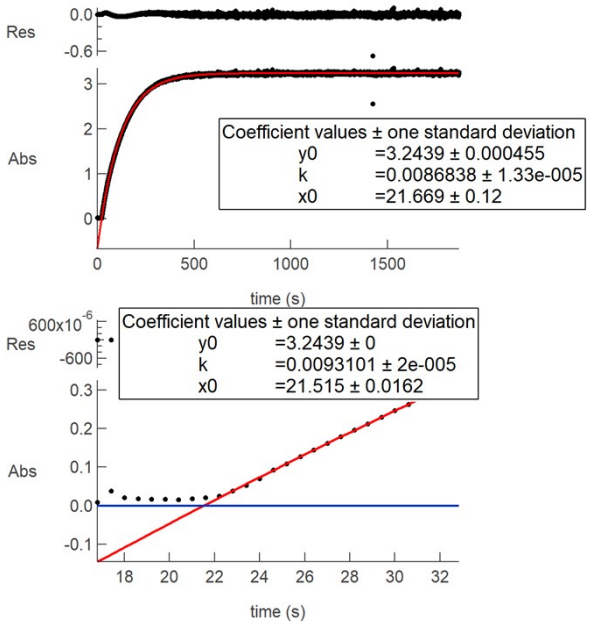

Expt. 55

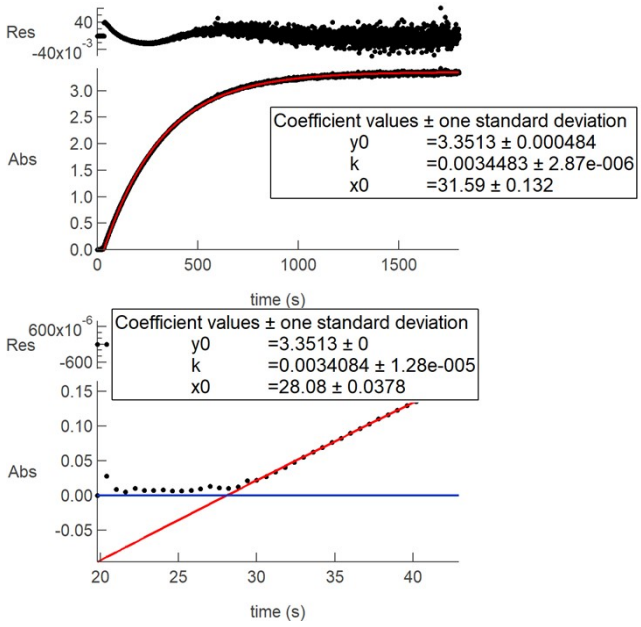

Expt. 56

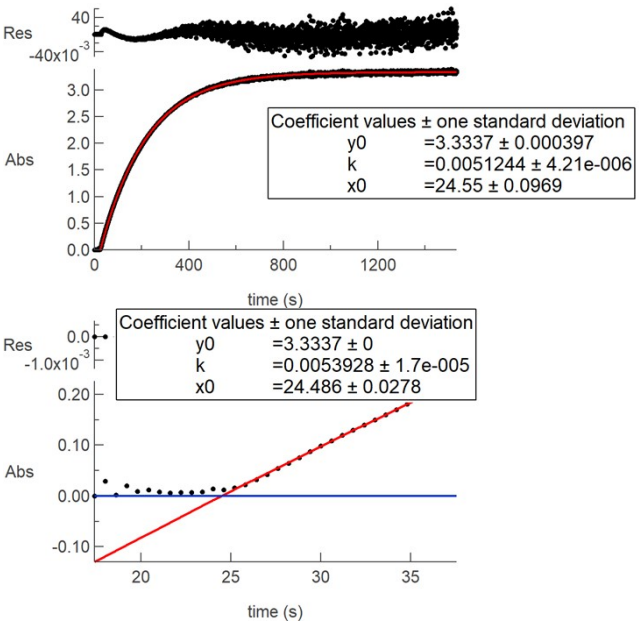

Expt. 57

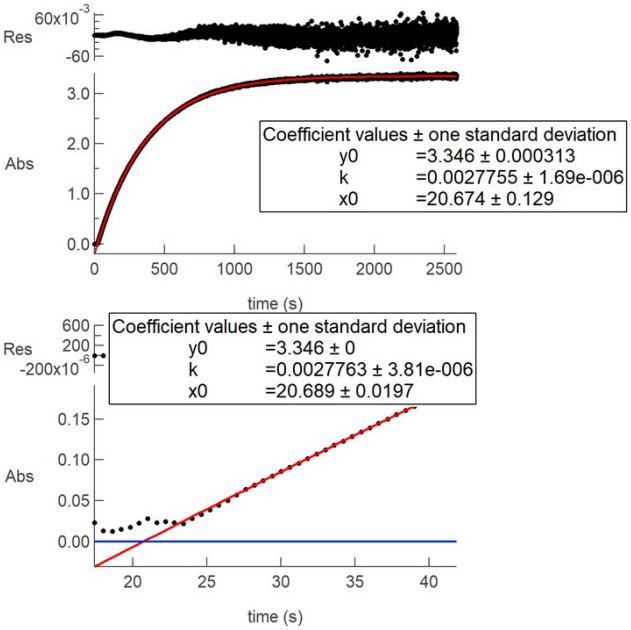

Expt. 58

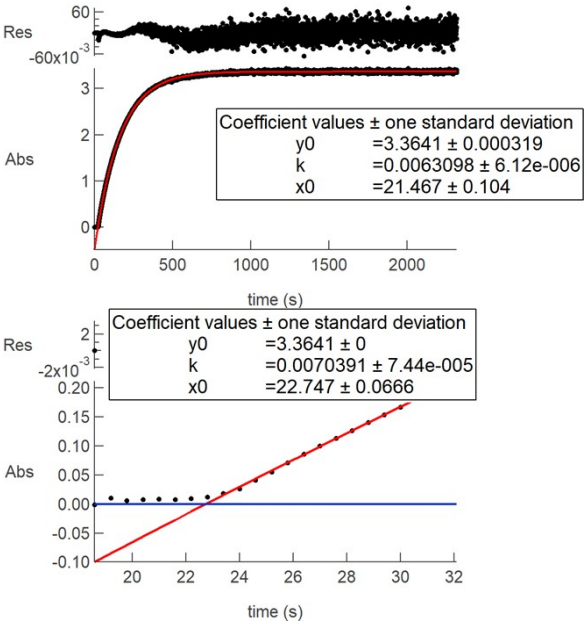

Expt. 59

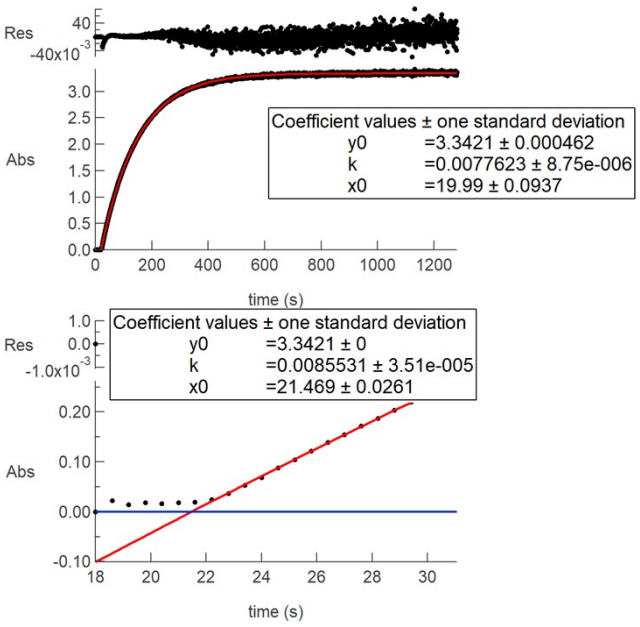

Expt. 60

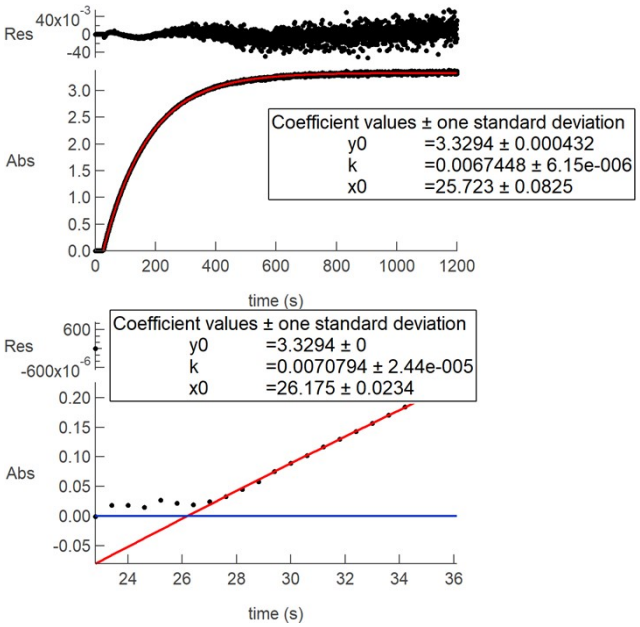

Expt. 61

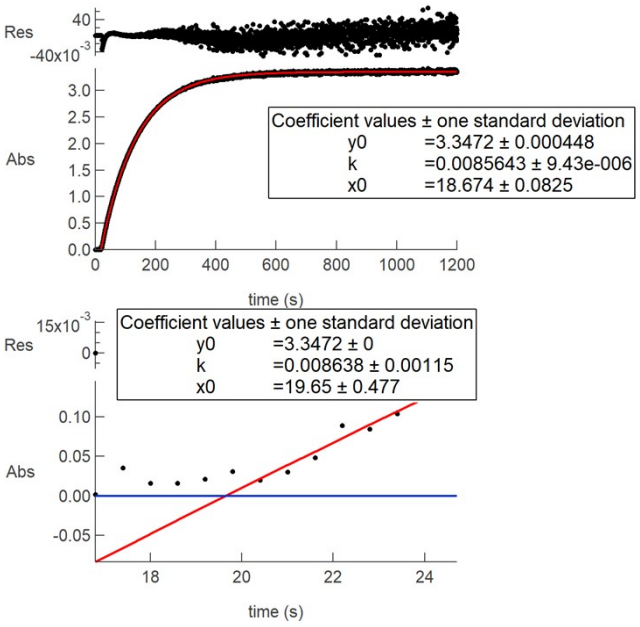

Expt. 62

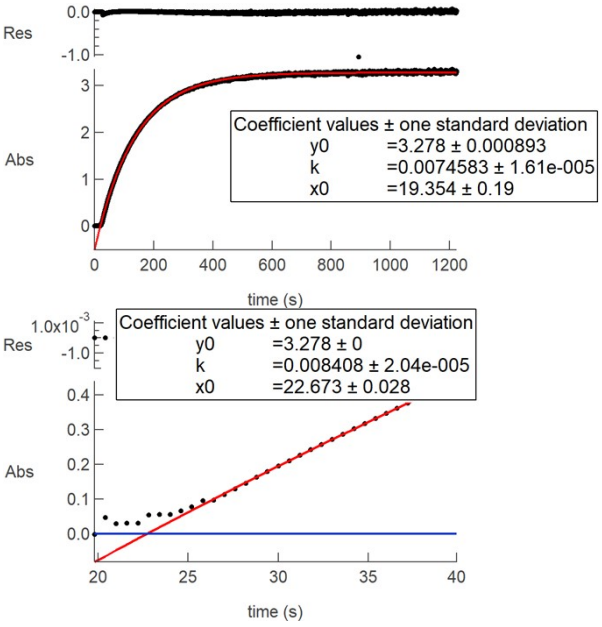

Expt. 63

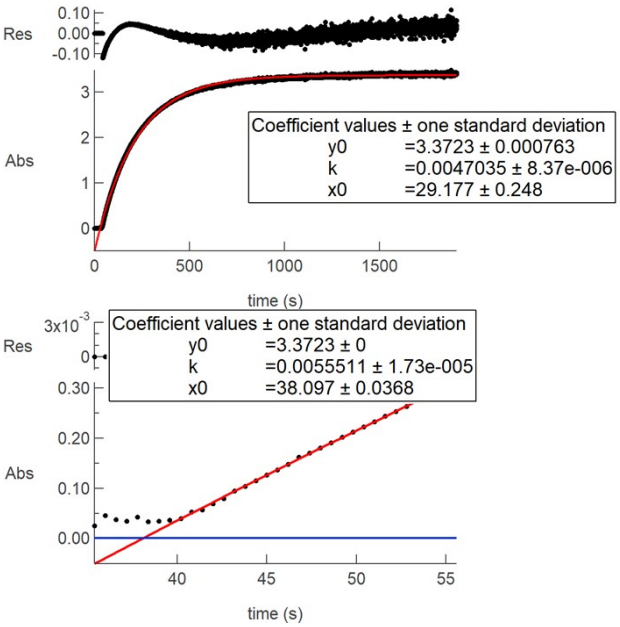

Expt. 64

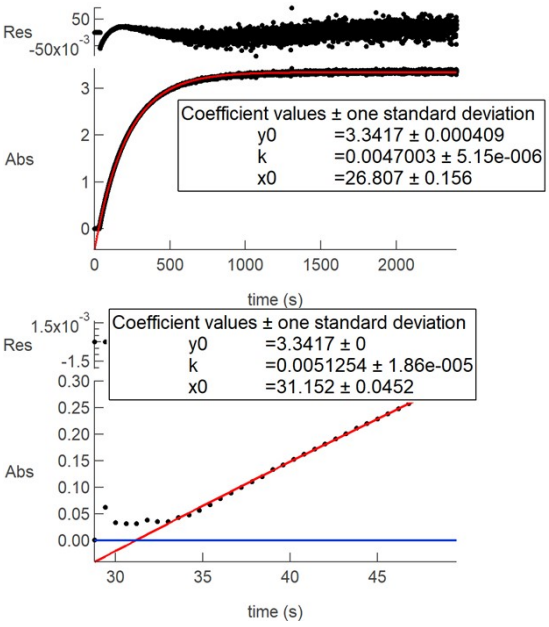

Expt. 65

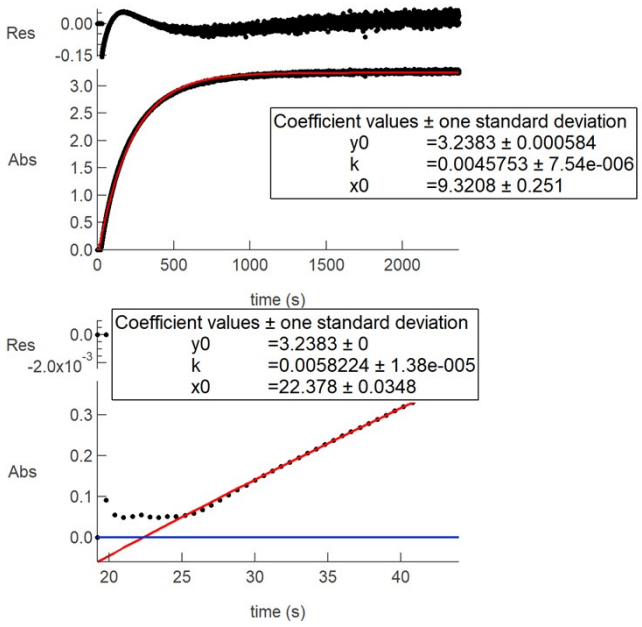

Expt. 66

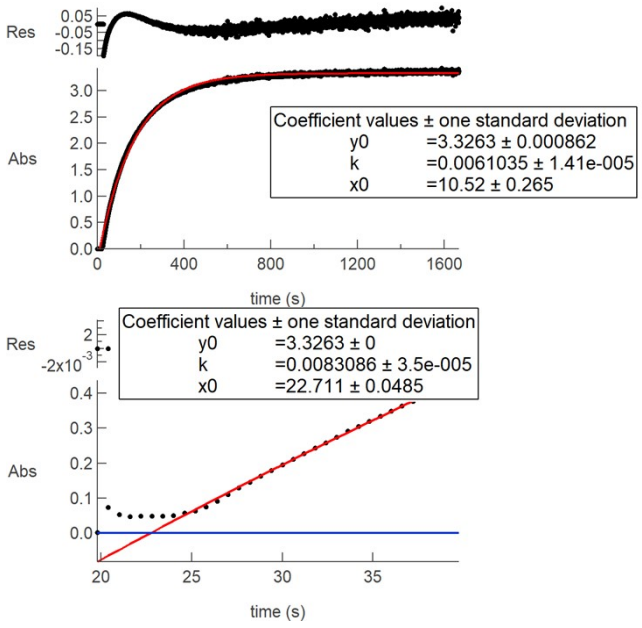

Expt. 67

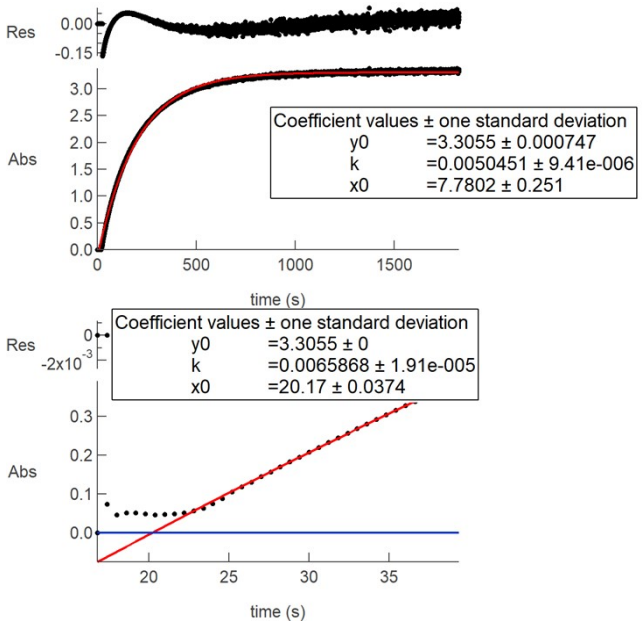

Expt. 68

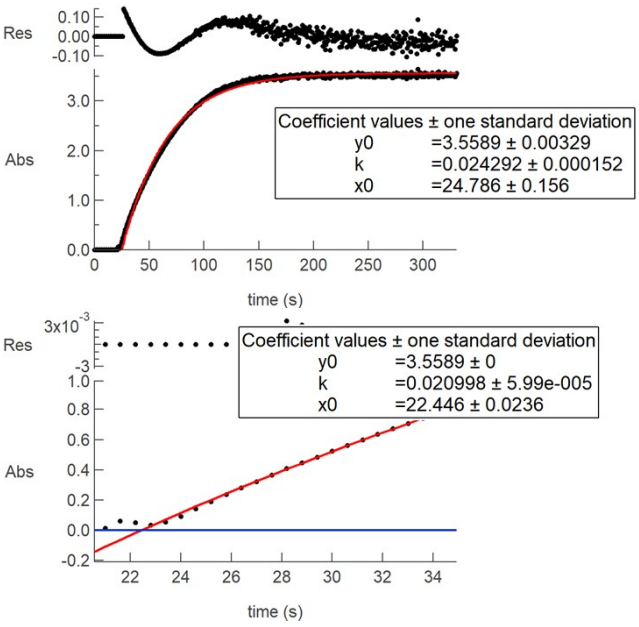

Expt. 69

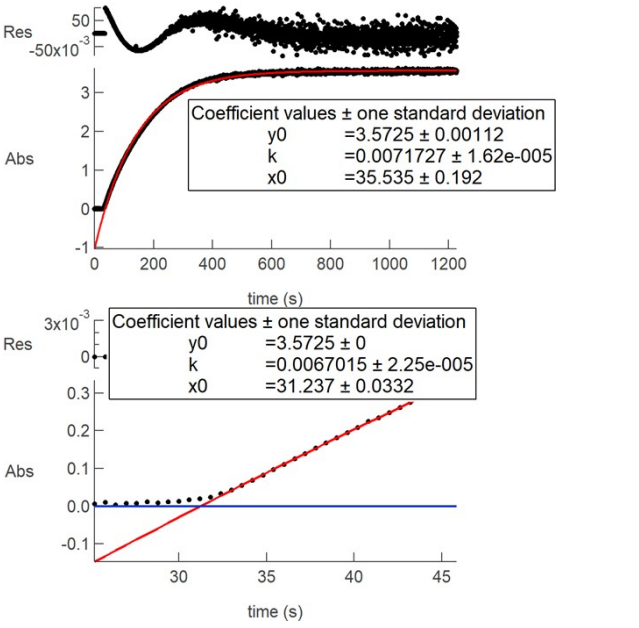

Expt. 70

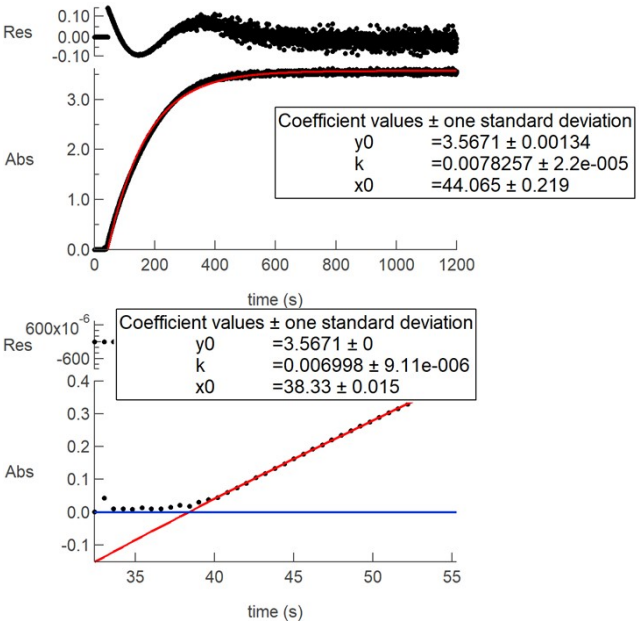

Expt. 71

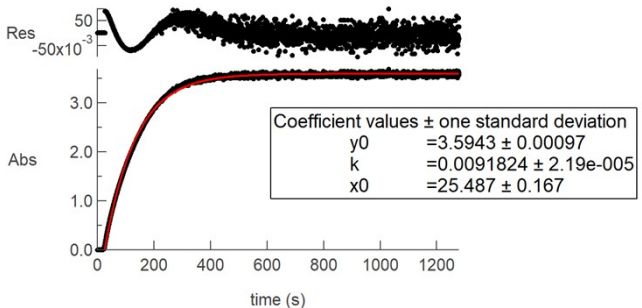

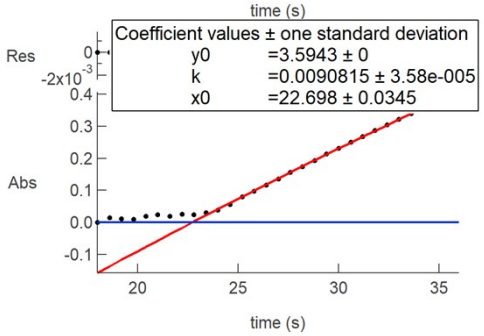

Expt. 72

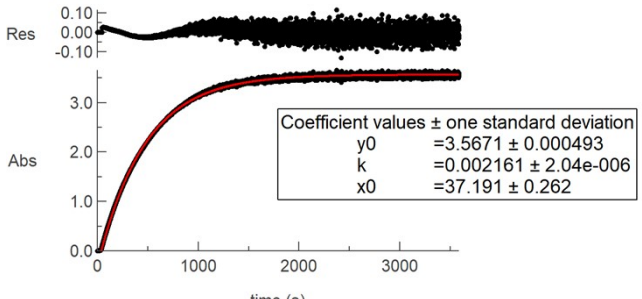

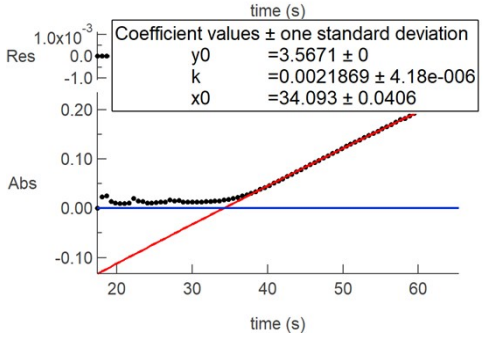

Expt. 73

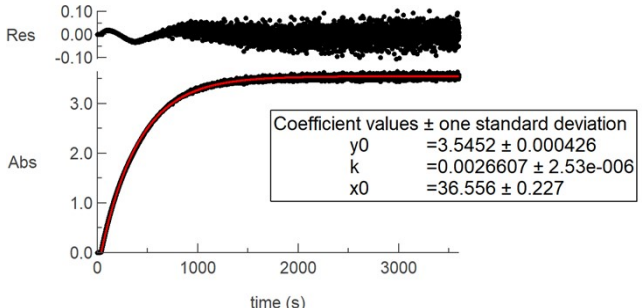

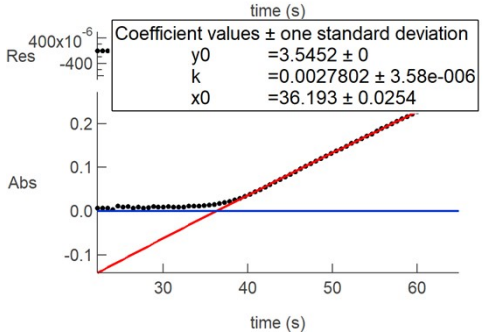

Expt. 74

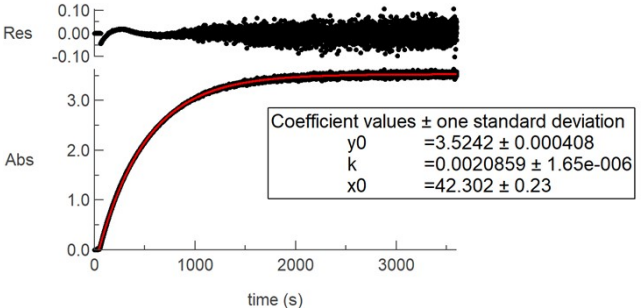

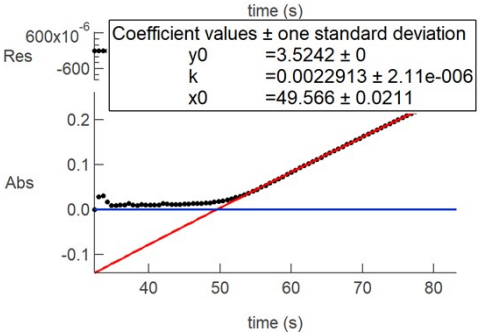

Expt. 75

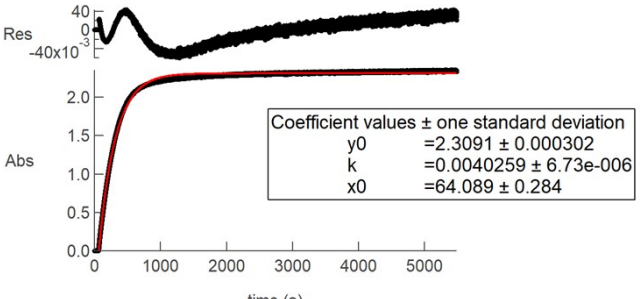

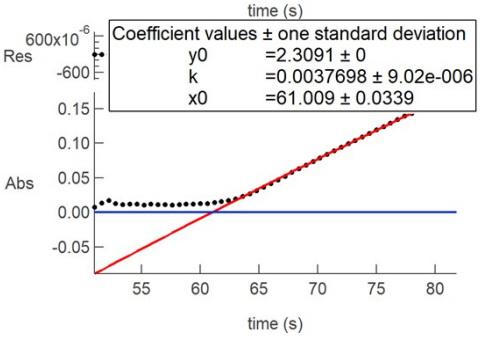

Section 10: References

1. Campos, M. P.; Hendricks, M. P.; Beecher, A. N.; Wslravens, W.; Swain, R. A.; Cleyeland, G. T.; Hens, Z.; Sfeir, M. Y.; Owen, J. S., A Library of Selenourea Precursors to PbSe Nanocrystals with Size Distributions near the Homogeneous Limit. *J Am Chem Soc* **2017**, *139*, 2296-2305.
2. Hendricks, M. P.; Campos, M. P.; Cleveland, G. T.; Jen-La Plante, I.; Owen, J. S., A tunable library of substituted thiourea precursors to metal sulfide nanocrystals. *Science* **2015**, *348*, 1226-1230.
3. Juhas, P.; Farrow, C. L.; Yang, X.; Knox, K. R.; Billinge, S. J., Complex modeling: a strategy and software program for combining multiple information sources to solve ill posed structure and nanostructure inverse problems. *Acta Crystallogr A Found Adv* **2015**, *71*, 562-8.
4. Bochevarov, A. D.; Harder, E.; Hughes, T. F.; Greenwood, J. R.; Braden, D. A.; Philipp, D. M.; Rinaldo, D.; Halls, M. D.; Zhang, J.; Friesner, R. A., Jaguar: A high-performance quantum chemistry software program with strengths in life and materials sciences. *Int J Quantum Chem* **2013**, *113*, 2110-2142.
5. Zhao, Y.; Truhlar, D. G., The M06 suite of density functionals for main group thermochemistry, thermochemical kinetics, noncovalent interactions, excited states, and transition elements: two new functionals and systematic testing of four M06-class functionals and 12 other functionals. *Theor Chem Acc* **2008**, *120*, 215-241.
6. Hanwell, M. D.; Curtis, D. E.; Lonie, D. C.; Vandermeersch, T.; Zurek, E.; Hutchison, G. R., Avogadro: an advanced semantic chemical editor, visualization, and analysis platform. *J Cheminformatics* **2012**, *4*.
7. Billinge, S. J. L.; Egami, T., Underneath the Bragg Peaks Structural Analysis of Complex Materials Concluding Remarks. *Pergamon Mater Ser* **2012**, *16*, 467-469.
8. Masadeh, A. S.; Bozin, E. S.; Farrow, C. L.; Paglia, G.; Juhas, P.; Billinge, S. J. L.; Karkamkar, A.; Kanatzidis, M. G., Quantitative size-dependent structure and strain determination of CdSe nanoparticles using atomic pair distribution function analysis. *Phys Rev B* **2007**, *76*.
9. Yang, X. H.; Masadeh, A. S.; McBride, J. R.; Bozin, E. S.; Rosenthal, S. J.; Billinge, S. J. L., Confirmation of disordered structure of ultrasmall CdSe nanoparticles from X-ray atomic pair distribution function analysis. *Phys Chem Chem Phys* **2013**, *15*, 8480-8486.
10. Kodama, K.; Iikubo, S.; Taguchi, T.; Shamoto, S., Finite size effects of nanoparticles on the atomic pair distribution functions. *Acta Crystallogr A* **2006**, *62*, 444-453.
11. Farrow, C. L.; Billinge, S. J. L., Relationship between the atomic pair distribution function and small-angle scattering: implications for modeling of nanoparticles. *Acta Crystallogr A* **2009**, *65*, 232-239.
12. Farrow, C. L.; Juhas, P.; Liu, J. W.; Bryndin, D.; Bozin, E. S.; Bloch, J.; Proffen, T.; Billinge, S. J. L., PDFfit2 and PDFgui: computer programs for studying nanostructure in crystals. *J Phys-Condens Mat* **2007**, *19*.
13. Abécassis, B.; Greenberg, M. W.; Bal, V.; McMurtry, B. M.; Campos, M. P.; Guillemeney, L.; Mehler, B.; Prevost, S.; Sharpnack, L.; Hendricks, M. P.; DeRosha, D.; Bennett, E.; Saenz, N.; Peters, B.; Owen, J. S., Monodisperse PbS Nanocrystals Following Persistent Nucleation and Size-dependent Growth. *Under Review*.
14. Norris, D. J.; Sacra, A.; Murray, C. B.; Bawendi, M. G., Measurement of the Size-Dependent Hole Spectrum in Cdse Quantum Dots. *Phys Rev Lett* **1994**, *72*, 2612-2615.
15. Hu, Y. Z.; Koch, S. W.; Lindberg, M.; Peyghambarian, N.; Pollock, E. L.; Abraham, F. F., Biexcitons in Semiconductor Quantum Dots. *Phys Rev Lett* **1990**, *64*, 1805-1807.
16. Klimov, V.; Hunsche, S.; Kurz, H., Biexciton Effects in Femtosecond Nonlinear Transmission of Semiconductor Quantum Dots. *Phys Rev B* **1994**, *50*, 8110-8113.

17. Ryu, J.; Jonas, D. M., Relations between absorption, emission and excited state chemical potentials from nanocrystal 2D spectra. *Sci Adv* **Accepted**.